

Evaluation of LPBF Steels for Nuclear Applications

Nuclear Science and Engineering Division

About Argonne National Laboratory

Argonne is a U.S. Department of Energy laboratory managed by UChicago Argonne, LLC under contract DE-AC02-06CH11357. The Laboratory's main facility is outside Chicago, at 9700 South Cass Avenue, Lemont, Illinois 60439. For information about Argonne and its pioneering science and technology programs, see www.anl.gov.

DOCUMENT AVAILABILITY

Online Access: U.S. Department of Energy (DOE) reports produced after 1991 and a growing number of pre-1991 documents are available free at OSTI.GOV (<http://www.osti.gov>), a service of the US Dept. of Energy's Office of Scientific and Technical Information.

Reports not in digital format may be purchased by the public from the National Technical Information Service (NTIS):

U.S. Department of Commerce
National Technical Information Service
5301 Shawnee Rd
Alexandria, VA 22312

www.ntis.gov

Phone: (800) 553-NTIS (6847) or (703) 605-6000

Fax: (703) 605-6900

Email: orders@ntis.gov

Reports not in digital format are available to DOE and DOE contractors from the Office of Scientific and Technical Information (OSTI):

U.S. Department of Energy
Office of Scientific and Technical Information
P.O. Box 62
Oak Ridge, TN 37831-0062

www.osti.gov

Phone: (865) 576-8401

Fax: (865) 576-5728

Email: reports@osti.gov

Disclaimer

This report was prepared as an account of work sponsored by an agency of the United States Government. Neither the United States Government nor any agency thereof, nor UChicago Argonne, LLC, nor any of their employees or officers, makes any warranty, express or implied, or assumes any legal liability or responsibility for the accuracy, completeness, or usefulness of any information, apparatus, product, or process disclosed, or represents that its use would not infringe privately owned rights. Reference herein to any specific commercial product, process, or service by trade name, trademark, manufacturer, or otherwise, does not necessarily constitute or imply its endorsement, recommendation, or favoring by the United States Government or any agency thereof. The views and opinions of document authors expressed herein do not necessarily state or reflect those of the United States Government or any agency thereof, Argonne National Laboratory, or UChicago Argonne, LLC.

Evaluation of LPBF Steels for Nuclear Applications

Prepared by

Srinivas Aditya Mantri
Xuan Zhang

Argonne National Laboratory

July 2023

Abstract

This report provides an update on the prioritization of existing reactor materials for advanced manufacturing. This report is a Milestone 3 deliverable in FY2023, under work package CT-23AN130401 to support research and qualification activities supported by the Advanced Materials and Manufacturing Technologies (AMMT) program here at Argonne National Laboratory (ANL). The focus of FY23 for ANL included the determination of a decision criteria matrix for the prioritization of existing materials, the literature review of a select few Fe-based alloys, and working with vendors to obtain customized powders. The work package also includes fabricating test samples in a Renishaw AM400 Laser Powder Bed Fusion (LPBF) system and optimizing the process parameters. The major outcomes of this work package are listed below.

- With collaborations from PNNL, ORNL, and INL, we were able to establish a decision criteria matrix containing a total of 6 categories and 31 different criteria. These will be used to downselect alloys for further evaluation.
- As part of that, 6 different Fe-based alloys were selected, 3 austenitic stainless steels (A709, D9, AFA) and 3 ferritic/martensitic steels (HT9, Grade 91, Grade 92). Customized powders were obtained from vendors in small quantities to fabricate initial prints to check printability of these specific alloys.
- A total of 72 single track experiments were performed on two alloy systems, 1 austenitic stainless steel (A709) and 1 ferritic/martensitic steel (Grade 91) in order to optimize the process parameters for the full 3d prints. The optimization led to the selection of 20 different processing conditions, 10 for each class of alloys.
- D9 and AFA alloys showed extensive cracking and porosity in the samples. This was due to less-than-ideal conditions present in the chamber during the deposition. A709 printed using the same process parameters showed almost fully dense samples with no noticeable porosity or any other defects. SEM and EBSD analysis revealed single phase FCC microstructure with cellular structure within the grains.
- HT9, Grade 91, Grade 92 alloys also showed no noticeable signs of cracking and ImageJ analysis showed porosity <0.5% in all conditions. While Grade 91 and Grade 92 showed single phase BCC microstructures, the presence of martensite laths was noted in HT9 alloy.

- Future work will include further characterization of these alloys to better understand the microstructural evolution during the 3d printing process.

Table of Contents

| | |
|--|-----|
| Abstract | i |
| Table of Contents | iii |
| List of Tables | iv |
| List of Figures | v |
| Introduction | 1 |
| Decision Criteria Matrix..... | 2 |
| Literature Review | 6 |
| 3.1 Introduction | 6 |
| 3.2 Austenitic Stainless Steels | 6 |
| 3.3 Ferritic/Martensitic Steels..... | 7 |
| Experimental Details | 9 |
| 4.1 Fabrication Technique | 9 |
| 4.2 Characterization Techniques..... | 9 |
| Results | 13 |
| 5.1 Single Track Experiments..... | 13 |
| 5.2 Full Builds | 14 |
| Discussions..... | 30 |
| 6.1 Single track experiment | 30 |
| 6.2 Block Build - Austenitic Stainless Steels | 31 |
| 6.3 Block Build - Ferritic/Martensitic Stainless Steels..... | 31 |
| Conclusions and Future Work | 33 |
| 7.1 Conclusions | 33 |
| 7.2 Future Work | 34 |
| Acknowledgements | 35 |
| Chapter 8: References | 36 |

List of Tables

| | |
|--|----|
| Table 1: Decision Criteria Matrix | 2 |
| Table 2: Optimized Process parameters for Austenitic Stainless Steels for the block build..... | 11 |
| Table 3: Optimized Process Parameters for Ferritic/Martensitic Steels for the block build..... | 12 |
| Table 4: Chemical composition of Austenitic Stainless-Steel alloys in wt.% | 12 |
| Table 5: Chemical composition of Ferritic/martensitic alloys in wt.% | 12 |

List of Figures

| | |
|---|----|
| Figure 1: Volumetric Energy Densities used for Single Track Experiments for (a) A-709 and (b)Grade 91 | 10 |
| Figure 2: Single track experiments on A709 alloy. In the highlighted image, the top layer shows single hatch spacing, while the bottom has double hatch spacing..... | 11 |
| Figure 3: Optical Images of cross section showing melt pools in single track experiments of A709 for recommended processing conditions for 316L SS..... | 13 |
| Figure 4: Optical Images of cross section showing melt pools in single track experiments of A709 for modified processing conditions. Red circles show the porosity in the samples. | 14 |
| Figure 5: SEM image showing the spherical D9 powders..... | 15 |
| Figure 6: Optical Images of 4 different processing conditions used for D9 alloy. Extensive cracking and other defects can be observed in all the conditions..... | 16 |
| Figure 7: SEM BSE image showing different features of sample condition 3 for D9 alloy. High magnification image in (d) shows cell structures noticed in other SS316 alloys. | 17 |
| Figure 8: EBSD IPF+IQ map showing grain size and orientation of D9 alloys. Build direction is indicated in the images..... | 17 |
| Figure 9: SEM image showing the spherical AFA powders. High magnification image showing artefacts. | 18 |
| Figure 10: Optical Images of 4 different processing conditions used for AFA alloy. Extensive cracking and other defects can be observed in all the conditions. | 18 |
| Figure 11: SEM image showing the spherical A709 powders..... | 19 |
| Figure 12: Optical Images of 4 different processing conditions used for A709 alloy. More than 99.5% density was achieved in all conditions. | 20 |

Figure 13: SEM BSE image showing different features of sample A709 alloy. High magnification images shows cell structures noticed in other SS316 alloys. 21

Figure 14: EBSD IPF+IQ map showing grain size and orientation of A709 alloys. No second phase is detected. 21

Figure 15: SEM image showing the spherical HT9 powders. 22

Figure 16: Optical Images of 4 different processing conditions used for HT9 alloy. More than 99.5% density was achieved in all conditions. 23

Figure 17: SEM BSE image showing different features of sample condition 3 for HT9 alloy. High magnification image shows clear presence of martensitic laths present in bcc matrix. 24

Figure 18: High magnification EBSD IPF+IQ map of HT9 alloy showing grain size and orientation. The un-indexed martensite laths can be seen in the bottom “orange” grain. 24

Figure 19: SEM image showing the spherical Grade 91 powders. 25

Figure 20: Optical Images of 4 different processing conditions used for Grade 91 alloy. More than 99.5% density was achieved in all conditions. 25

Figure 21: SEM BSE image showing different features of sample condition 9 for Grade 91 alloy. No martensite was noted in this alloy, though very small cells were present throughout. 26

Figure 22: High magnification EBSD IPF+IQ map of sample condition 9 for Grade 91 alloy showing grain size and orientation. No secondary phase is detected. 27

Figure 23: SEM image showing the spherical Grade 92 powder. 28

Figure 24: Optical Images of 4 different processing conditions used for Grade 92 alloy. More than 99.5% density was achieved in all conditions. 28

Figure 25: SEM BSE image showing different features of sample condition 7 for Grade 92 alloy. No martensite was noted in this alloy, though very small cells were present throughout. 29

Figure 26: Schematic showing the melt pool overlap and effects of energy density.[33] 30

Introduction

Additive Manufacturing is a process of fabricating objects via a layer-by-layer deposition from a 3d geometry model into complex near net shape components, thus reducing the need for post process machining, welding, and brazing[1]. Recently, there has been a huge push to explore the feasibility of using additive manufacturing techniques for the fabrication of components in energy industries[2], [3]. Of particular interest for the current project, based on the AMMT roadmap, is the incorporation of current reactor materials[4]. Four US national labs, ANL, INL, ORNL, and PNNL will work on selecting current reactor materials that have a potential to benefit from additive manufacturing. A key goal of the work package is to establish a design criteria matrix for assessment of all potential materials of interest. Following this, once an initial down-selection of alloys is completed, the key alloys will be fabricated via Laser Powder Bed Fusion (LPBF) techniques to check the printability. The current report summarizes both the aforementioned design criteria matrix and the initial study of the alloys chosen. In collaboration with PNNL, ANL worked on Fe-based alloys which will be reflected in the report.

Chapter 2 will give insights into the decision criteria matrix and will expand on the six categories chosen. Based on the decision criteria matrix, 6 alloys were chosen: D9, AFA, A709, HT9, Grade 91, and Grade 92. Chapter 3 will provide a literature review of LPBF techniques and a more in-depth review of the alloys downselected. Following this chapter 4 discusses the experimental details relevant to the present work, including information about the fabrication techniques as well as the characterization techniques.

In the next 3 chapters, there will be discussion of the current results, followed by conclusions and finally future work that needs to be performed. A final summary will also be provided at the end of the report.

Decision Criteria Matrix

In order to ensure that there is a transparent and consistent decision process for the selection of reactor materials for advanced manufacturing, it is very important to have a determination of relevant criteria. PNNL created some early score cards[4], based on available literature data, industry response to a survey, input from stakeholders collected at workshops, and expert opinion, for the following nuclear alloys: 316SS, SS304, Alloy 800H, Graphite C/C, Alloy N, Silicon Carbide, HT9, Alloy 617, and Alloy 718. Code availability, Gaps in data availability for performance values and measurements, technical maturity for end use/development stage, deployment readiness requirements, supply chain availability and programmatic factors were the six key categories considered when evaluating each material. 316 and 304 stainless steels obtained the highest ranking and 316H is now the focus of the AMMT program. To further expand the process and take advantage of the expertise at the four participating national laboratories, recurrent meetings were organized to discuss, select, and rank a broader range of reactor materials under a modified decision criteria matrix. The current decision matrix containing a total of 34 criteria, divided into 6 key categories is shown in Table 1. The matrix was presented at several review meetings and at an industrial workshop at ORNL and modified based on participants’ feedback. With more feedback from stakeholders, this matrix is expected to evolve with time. The definition and relevance of each individual key category is further discussed in this section.

Table 1: Decision Criteria Matrix

| Category | Criteria | | | | | | | | | | | |
|-----------------------------------|----------------------|-------|------------------------------------|-------|------------------------------------|-------|-----------------------------------|-------|-----------------------------|-------|-------------------|---|
| | Score | Score | Score | Score | Score | Score | Score | Score | Score | Score | | |
| Manufacturing/Powder | Powder Availability | 4 | Powder Properties | 2 | Powder Chemistry | 3 | Cost | 2 | Recycling | 2 | | |
| Manufacturing/Components | Printability (LBF) | 5 | Defects | 4 | Post Treatment | 3 | Processing window | 4 | Weldability | 3 | Surface Roughness | 2 |
| History & Applications | NE Experience | 4 | Other Industries Experience | 3 | Data availability | 4 | Code Data Availability | 4 | Experience with non-LPBF AM | 2 | Surface Finish | 2 |
| Mechanical Properties | Creep | 4 | Fatigue | 3 | Creep-fatigue | 3 | High Temp tensile strength | 2 | Room Temp | 2 | Scaling Up | 3 |
| Environmental Effects | Radiation Resistance | 5 | Oxidation Resistance | 2 | Stress Corrosion Cracking | 2 | Molten Salt | 3 | Liquid Metal | | | |
| Physical Properties | Thermal Properties | 2 | Solidification-relevant properties | 2 | Other modeling-relevant properties | | Digital Manu. relevant-properties | | | | | |
| Microstructure | Material Homogeneity | 3 | Microstructure Stability | 3 | LPBF Microstructure Specificity | 2 | | | | | | |

Manufacturing (Powder and Components)

One of the major roadblocks in exploring new alloy systems for additive manufacturing is powder. While most materials are available in wrought or cast form, few powders are available commercially. While using customized powders is an option, these usually have a minimum quantity requirement and a very long lead time. Even if the powder is obtained, there are multiple other factors which need to be explored/understood. Powder flowability, which is determined by the process used (LPBF vs DED) plays a key role in getting a good build. Powder chemistry needs to be as close to specifications of the alloys. The high cooling rates in AM builds lead to specific non-equilibrium microstructure and variation of the alloy chemistry within the alloy specification and may have an impact on the alloy microstructure and properties[1], [5]. The cost of powders is also a very important criterion which needs to be taken into consideration as most of the customized powders could lead to higher costs. The recyclability of the powders also goes hand-in-hand with the cost of the powders. Alloy powders which can be recycled and reused will lower the overall cost.

Printability is also an important consideration. Building a crack-free high-density material is of the highest priority. The other things to consider with the AM prints are the processing window (a wide range = better material), weldability (goes hand-in-hand with printability and cracking), surface roughness and finish (important for fatigue, creep fatigue among other things), and post fabrication/printing heat treatments. The microstructure after the heat treatments should ideally be like what is necessary for the application.

History and Applications

The major criteria to consider here are similar to what was mentioned in the PNNL scorecards. A material which is known to be used for not only nuclear energy applications, but also for other industries, e.g., fossil fuel, will rank higher in the matrix. This can also be termed as having a cross-industry appeal. Materials for which data availability and code data availability in terms of microstructures, mechanical properties, irradiation properties, and corrosion among other properties will merit a higher ranking in the decision criteria matrix. Scalability will also play a role in the matrix, but it is assumed, based on the literature, this is not a major factor.

Mechanical Properties

The mechanical properties of the materials to be manufactured via AM are of increased importance in the decision-making process. Creep, fatigue, and creep fatigue rank higher in the matrix as they

are considered more important than room temperature mechanical properties for the specific applications in advanced nuclear reactors. A material with better creep properties will be ranked higher than a material with better room temperature properties.

Environmental Effects

Resistance to radiation is of high importance when considering materials for nuclear energy applications. As such, a rating of 5 was assigned to this criterion, i.e., the alloy selected should have very high tolerance to radiation. Oxidation resistance, stress corrosion cracking, corrosion resistance (depending on the reactor type: molten salt, liquid metal etc.) are also considered in the decision matrix but are not ranked as high as radiation resistance.

Physical Properties

Physical Properties like thermal properties (expansion, conductivity) are also considered as they affect the printability of the alloy and also the homogeneity of the microstructure throughout the build. Similar to the thermal properties, solidification-relevant properties are also important as they determine the grain structure of the 3D printed alloys.

Microstructure

The microstructure of the 3D printed alloys plays a major role in the overall applications. The major factors considered in this category were material homogeneity (same microstructure throughout the build) and microstructure stability (the microstructure does not change too much or disintegrate at elevated operating temperatures). The grain structures, precipitation, and dislocation structures are also important factors as they critically impact the materials' performance.

Result of the Decision Criteria Matrix

Based on the decision matrix criteria, a few alloys were chosen. While ORNL and INL will work on Ni-based alloys, ANL and PNNL will work on Fe-based alloys. A total of 6 different types of stainless steels, 3 austenitic and 3 ferritic/martensitic, were selected for initial assessment, literature review, 3D printing, and microstructural characterization. A brief explanation on the selection of these specific alloys is provided below. The literature review in the following sections will go into more details.

Austenitic Stainless Steels:

1. A709: A lot of literature is available for wrought A709, and it is one of the next alloys being considered for code qualification. No work on AM done so far, and powder is not available commercially. The other major consideration point is that it has cross-industry appeal.
2. D9 (Titanium Modified Stainless Steel): D9 steel is a modified version of SS316L with 3-6 times Ti added as a percentage of carbon. The formation of TiC particles and their interfaces with the matrix serve as sinks for the radiation induced point defects and thus contribute to enhancing the swelling resistance of alloy. As the alloy composition is very close to SS316L, the vast knowledge obtained from the 3D printing data can be implemented here. Powder is not commercially available, and no AM work has been performed.
3. Alumina Forming Austenitic (AFA) Steel: Cross-industry appeal. Better SCC properties than SS-316. Powder is not available commercially, and very little AM work has been performed.

Ferritic/Martensitic Steels:

1. 9Cr alloys: Grade 91 (9Cr-1Mo) is a code qualified alloy which makes it a strong candidate for consideration. There is extensive work on the commercial alloys and substantial work is being done on the AM samples too. Grade 92 (9Cr-2W-0.5Mo) is a variation of Grade 91 with tungsten added to increase the overall creep strength. Currently there is no available literature on the AM of Grade 92 alloy.
2. HT9: HT9 (12Cr-1Mo) was a key alloy in the PNNL scorecards. Significant work has been done on the bulk alloys which can play an important role in understanding the overall microstructural evolution of AM alloys. This alloy also has a significant cross-industry appeal. There are only a few papers available on the AM of this alloy.

Literature Review

3.1 Introduction

As mentioned in the previous section, based on the decision matrix, ANL focuses on two main classes of steels as part of the current work package: (i) Austenitic Stainless Steels, (ii) Ferritic/Martensitic steels. The following section gives a brief overview of the alloys considered.

3.2 Austenitic Stainless Steels

3.2.1 *A709(NF709)*

First developed by the British in 1950s, the 20Cr25Ni/Nb stainless steel has been used as a fuel cladding material for the British Advanced Gas-cooled Reactor (AGR) fleet since 1962[6]. Approximately 90,000 fuel pins were present in each AGR plant, and there were 14 plants constructed and operated. While the creep strength of 20Cr25Ni/Nb was relatively low, it was sufficient for its intended application. Based off this, in the 1980s, the Nippon Steel Corporation modified the base chemical composition by adding B, Mo, and Ti to 20Cr25Ni/Nb in order to strengthen the creep resistance for ultra-supercritical boilers. The resulting austenitic stainless steel was trademarked NF 709[7]. The design criteria for developing the composition of NF 709 were to have a stable austenite devoid of the sigma and other intermetallic phases under long-term elevated-temperature service conditions, and creep-strengthened by carbonitride M(CN) precipitated in a stable, fine dispersion. Through a DOE-NE ART material down-selection and intermediate term testing program, Alloy 709, an advanced austenitic stainless-steel alloy, was recommended as a Class A structural material for the SFR because of its overall superior structural strength advantage[8], [9]. While extensive work has been performed on A709 in the wrought form to have it code-qualified, there is no available literature on the additive manufacturing aspect.

3.2.2 *D9 (Ti-modified stainless steel)*

The D9 alloy is a titanium-modified, 316 stainless steel which has provided improved resistance to neutron irradiation induced void swelling as compared with the unmodified 316 stainless steel[10]– [12]. The addition of Ti in the matrix is crucial for binding a portion of the dissolved carbon in the form of tiny TiC precipitates. It is believed that the TiC-matrix interfaces serve as sinks for radiation induced point defects and enhance the swelling resistance[13]. The formation of chromium carbides is also reduced, thus improving the overall corrosion resistance. Most of the

work on bulk form of D9 was done in the early 90s. Recently there have been few publications on the effect of addition of Ti to stainless steels via directed energy deposition. The alloying here was done in-situ, i.e., titanium was added independently. The addition of Ti to SS316 was noted to refine the grains and increase the overall tensile strengths[14], [15]. Currently, there isn't any available data on the laser bed powder fusion of D9 alloy.

3.3 Ferritic/Martensitic Steels

3.3.1 HT9

Sandvik HT9 was the first ferritic/martensitic steel considered in the US Fusion Materials Program when it was decided to investigate these steels as structural materials for the first wall and blanket structures of fusion reactors[16]. The rich irradiated materials database on HT9 has prompted commercial startup companies such as TerraPower LLC to revitalize the manufacturing of HT9[17]. The adequate in-core performance of HT9 has also been demonstrated by its successful applications as fuel cladding and ducts in Fast Flux Test Facility (FFTF). The most critical issue that may limit the usage of HT9 in future nuclear energy systems is its irradiation embrittlement at low temperatures. A significant shift in DBTT above 120°C can be observed after neutron irradiation below 400°C[18]. ORNL published a series of papers on the additively manufactured HT9, but all the work they did was on the blown powder technique. The characterization showed that the as-built structure essentially consisted of a martensitic matrix with δ -ferrite present in the reheat zones between each pass during the sample fabrication process[19]–[21]. The martensitic matrix consisted of an ultrafine dispersion of carbides and carbonitrides. Currently, there is no available literature on the LPBF of HT9 alloy.

3.3.2 Grade 91

Grade 91 steel was developed as a 2nd generation creep resistant alloy. ORNL modified the composition by adding small amounts of V and Nb to 9Cr–1Mo to form fine carbo-nitrides[16]. Broadly used in fossil and nuclear power plants in components operating at temperatures up to ~650°C, it is the current “workhorse” alloy and the only alloy being studied in the current work package which is included in ASME Boiler and Pressure Vessel (B&PV) Code Section III Division 5 [22]. Having a Cr concentration of 9 wt% gives very good creep strength while having a minimal increase in the DBTT. Significant work has been performed recently on the additive manufacturing of Grade 91 steel. Blown powder technique, wire DED, and LPBF based techniques have all been used to fabricate this alloy to understand the microstructural evolution, mechanical behavior,

corrosion, and in some cases even irradiation behavior[23]–[26]. In the case of LPBF sample, as-deposited additively manufactured Grade 91 steel had a microstructure of lower bainitic regions surrounded by martensite. The as-deposited additively manufactured material had excellent tensile mechanical properties with greater strength than the wrought material at room and elevated temperatures, showing excellent promise for nuclear applications. Retention of strength at 300 and 600 °C for the as-deposited additively manufactured material was attributed to transitional carbides in the lower bainitic regions[27], [28].

3.3.3 Grade 92

To improve the creep properties of 2nd generation Grade 91 alloy, Grade 92 steel was developed as a 3rd generation creep-resistant F/M steel with the addition of tungsten and minute amounts of boron. While it has been reported to have better creep properties relative to Grade 91, it has not been code qualified[16], [29]. In practice, the microstructure is made up of tempered martensitic lath structure which is stabilized by Cr rich $M_{23}C_6$ carbide, intra-lath MX type of Nb and V carbonitrides, martensite phase transformation induced high dislocation density, and solid solution strengthening from tungsten[30], [31]. The presence of tungsten in the $M_{23}C_6$ precipitate decreases growth rate of the precipitate during creep exposure, which in turn increases the stability of the martensitic lath structure of the steel on creep exposure. Currently, there is no available research on the additive manufacturing of Grade 92 steel.

Experimental Details

4.1 Fabrication Technique

A Renishaw AM400 LPBF machine equipped with a reduced build volume was used to fabricate all the samples. The machine is equipped with a Yb-Fiber pulsed laser with a maximum power of 400W and a beam diameter of 70 microns. In order to optimize the process parameters, single track experiments were performed on two of the alloys: an austenitic stainless steel (A709) and a ferritic/martensitic steel (G91). A total of 72 parameter sets were initially planned for these systems. Laser power, exposure time, and point distance were varied. The parameters of A709 were based on the literature review and from Renishaw (based on SS-316L). The recommended condition from Renishaw is highlighted with a *star* in Fig. 1(a). The parameters for G-91 were based on literature review, experimental evidence from LANL, and from Renishaw (based on 17-4PH Steel). The process parameters are shown in Figure 1 and a fully processed single track image is shown in Figure 2. Based on this study, a total of 10 block samples with different processing conditions were built for each of the 6 alloys, depending on the alloy class, i.e., austenitic stainless steels vs ferritic/martensitic steels. The process parameters are in Tables 2 and 3. The powders were manufactured by the company Atlantic Equipment Engineers (AEE) using argon gas atomization in 15-20 kg batches. The compositions of the powders are listed in Tables 4 and 5. Each sample was printed to be a 10mm*10mm*10mm cube.

4.2 Characterization Techniques

Once the samples were printed, they were sectioned along the build direction to study the microstructure. Standard metallography techniques were employed to polish the samples for optical and electron microscopes. Samples were polished to 4000 grit SiC abrasive paper, followed by diamond suspension (3 μm and 1 μm), and by a 0.05 μm colloidal silica suspension final polish in a Buehler Vibromet. The samples for single-track experiments were etched with a 30 ml H_2O , 30 ml HCl, 10 ml HNO_3 mixture to reveal the melt pool. Optical microscopy was done on a Keyence VHX-970F Digital Microscope. Three micrographs were taken for each sample (60 samples overall) and were analyzed in ImageJ to calculate the porosity. A JEOL 7500 SEM was used for electron microscopy, EBSD, and EDS.

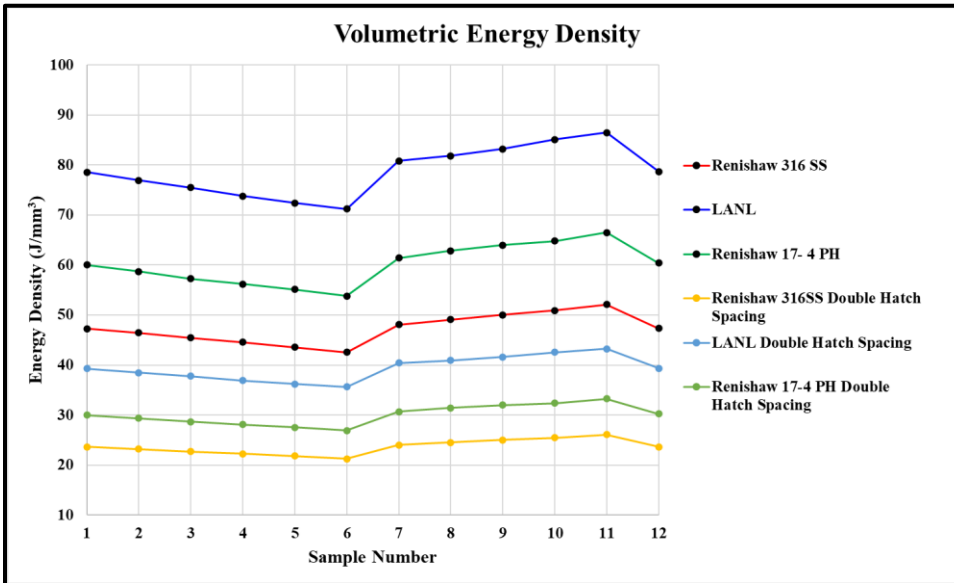
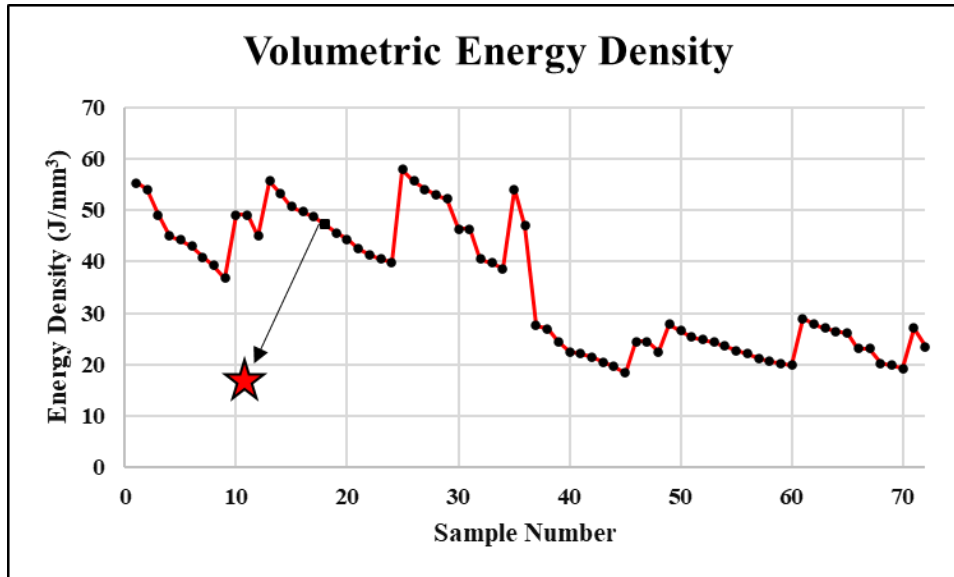


Figure 1: Volumetric Energy Densities used for Single Track Experiments for (a) A-709 and (b) Grade 91

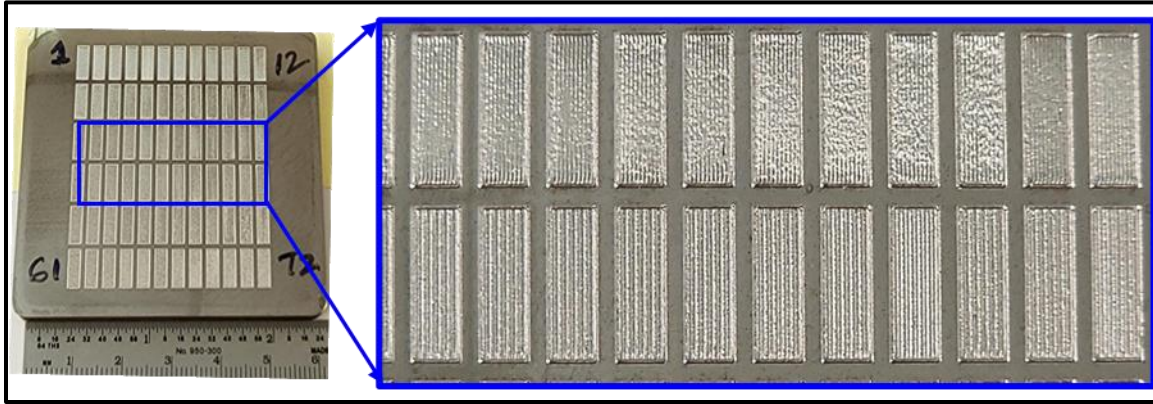


Figure 2: Single track experiments on A709 alloy. In the highlighted image, the top layer shows single hatch spacing, while the bottom has double hatch spacing.

Table 2: Optimized Process parameters for Austenitic Stainless Steels for the block build.

| Sample | Laser Power (W) | Exposure Time (μ s) | Hatch Space (μ m) | Point Distance (μ m) | Layer Thickness (μ m) | Energy Density (J/mm^3) |
|--------|-----------------|--------------------------|------------------------|---------------------------|----------------------------|-----------------------------|
| 1 | 195 | 70 | 110 | 50 | 50 | 49.63 |
| 2 | 195 | 110 | 110 | 80 | 50 | 48.75 |
| 3 | 195 | 80 | 110 | 60 | 50 | 47.27 |
| 4 | 195 | 90 | 110 | 70 | 50 | 45.58 |
| 5 | 195 | 100 | 110 | 80 | 50 | 44.31 |
| 6 | 215 | 90 | 110 | 70 | 50 | 50.25 |
| 7 | 215 | 100 | 110 | 80 | 50 | 48.86 |
| 8 | 215 | 60 | 110 | 50 | 50 | 46.90 |
| 9 | 215 | 70 | 110 | 60 | 50 | 45.60 |
| 10 | 215 | 80 | 110 | 70 | 50 | 44.67 |

Table 3: Optimized Process Parameters for Ferritic/Martensitic Steels for the block build.

| Sample | Laser Power (W) | Exposure Time (μs) | Hatch Space (μm) | Point Distance (μm) | Layer Thickness (μm) | Energy Density (J/mm ³) |
|--------|-----------------|--------------------|------------------|---------------------|----------------------|-------------------------------------|
| 1 | 221 | 101 | 110 | 55 | 50 | 73.78 |
| 2 | 185 | 101 | 110 | 45 | 50 | 75.49 |
| 3 | 270 | 80 | 110 | 50 | 50 | 78.54 |
| 4 | 200 | 100 | 110 | 45 | 50 | 80.80 |
| 5 | 305 | 75 | 110 | 50 | 50 | 83.18 |
| 6 | 165 | 105 | 110 | 55 | 50 | 57.27 |
| 7 | 220 | 62 | 110 | 45 | 50 | 55.11 |
| 8 | 180 | 110 | 110 | 60 | 50 | 60 |
| 9 | 200 | 95 | 110 | 55 | 50 | 62.80 |
| 10 | 225 | 95 | 110 | 60 | 50 | 64.77 |

The final compositions of the powder obtained from the company Atlantic Equipment Engineers is listed below.

Table 4: Chemical composition of Austenitic Stainless-Steel alloys in wt.%

| Alloy | Fe | Cr | Ni | Mn | Mo | C | N | Si | Ti | Nb | Al |
|----------|------|------|------|------|------|------|------|------|------|------|-----|
| D9 Steel | Bal. | 13.7 | 14.9 | 1.9 | 2.2 | 0.04 | n/a | 0.6 | 0.26 | n/a | n/a |
| AFA | Bal. | 12.7 | 19.2 | 0.03 | 2.18 | 0.02 | n/a | 0.4 | n/a | 0.78 | 2.3 |
| A709 | Bal. | 20 | 25.4 | 0.91 | 1.51 | 0.06 | 0.16 | 0.44 | 0.04 | 0.26 | n/a |

Table 5: Chemical composition of Ferritic/martensitic alloys in wt.%

| Alloy | Fe | Cr | Mo | Mn | W | V | Nb | C | Ni | Si | N |
|----------|------|-----|-----|------|-----|------|------|-----|------|------|-----|
| HT9 | Bal. | 12 | 1 | n/a | 0.5 | 0.25 | n/a | 0.2 | n/a | 0.21 | n/a |
| Grade 91 | Bal. | 8.3 | 0.9 | 0.43 | n/a | 0.2 | 0.06 | 0.1 | 0.17 | 0.42 | n/a |

| | | | | | | | | | | | |
|----------|------|-----|-----|------|-----|-----|------|------|-----|------|-----|
| Grade 92 | Bal. | 8.7 | 0.5 | 0.45 | 1.9 | 0.2 | 0.07 | 0.09 | n/a | 0.14 | n/a |
|----------|------|-----|-----|------|-----|-----|------|------|-----|------|-----|

Results

5.1 Single Track Experiments

The idea behind performing single track experiments was to optimize the process parameters while we waited on the powders. A total of 72 different processing conditions were used for each of the alloy systems, i.e., A709 for austenitic stainless steels and Grade 91 for F/M steels. Figure 3 shows the cross section of A709 for one of the ideal conditions given by Renishaw.

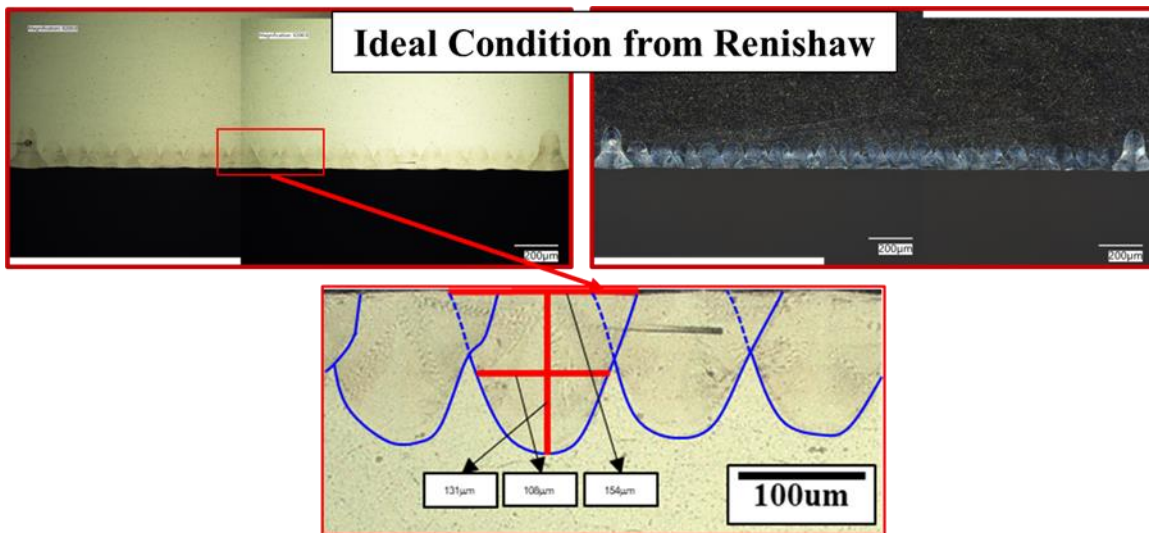


Figure 3: Optical Images of cross section showing melt pools in single track experiments of A709 for recommended processing conditions for 316L SS.

In comparison to the ideal condition for 316L SS provided by Renishaw, another example is provided and shown in Figure 4 where keyhole effects can clearly be observed.

Based off these results, we were able to narrow down processing conditions to 10 for each of the alloy systems.

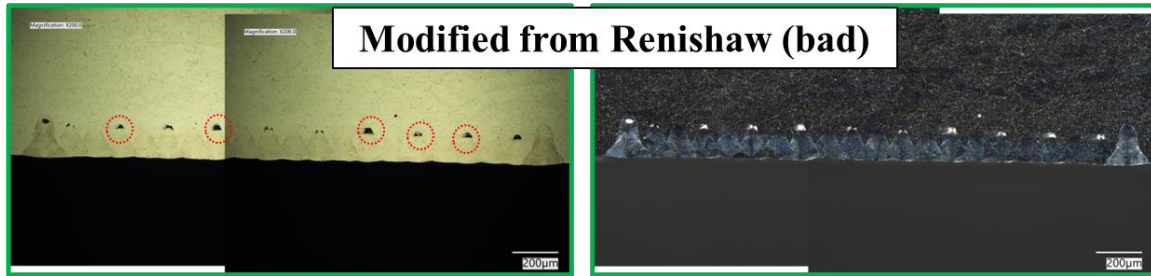


Figure 4: Optical Images of cross section showing melt pools in single track experiments of A709 for modified processing conditions. Red circles show the porosity in the samples.

5.2 Full Builds

The results from each alloy will be presented following the same structure. A small introduction about the powders will be followed by optical imaging, showing porosity and other possible defects, and then by scanning electron microscopy showing high magnification microstructures and electron backscattered diffraction images.

5.2.1 Austenitic Stainless Steels

5.2.1.1 D9 (Ti-modified Stainless Steel)

Figure 5 shows the as received D9 powder with a higher magnification image shown in the inset. The powder can be seen to be spherical, though a few planetary powders can be seen. This form of powder typically has a high packing density as the small voids in the large particles are filled by the small particles, and it also optimized the fluidity and stacking density, which is very suitable for additive manufacturing[1].

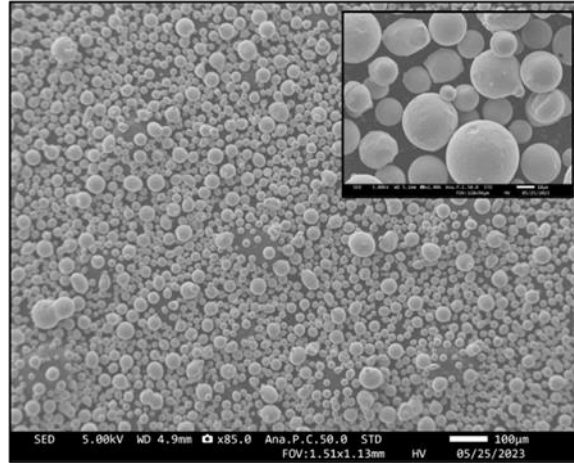


Figure 5: SEM image showing the spherical D9 powders.

Following the deposition, the samples were sectioned in half and the microstructures were observed along the build direction. While optical imaging was done for all 10 samples, for conciseness, Figure 6 shows a few select conditions. As can be seen in the images here, there are a high number of cracks along the grain boundaries, parallel to the build direction. Most of the cracking observed here is along the grain boundaries with a very minimal amount noted in the interiors. It should be noted here that during the deposition of D9 and AFA (will be discussed in next section), there was a vacuum leak in the Renishaw system which possibly could have led to

the defects observed in the current microstructures. We are currently investigating further to isolate the issue.

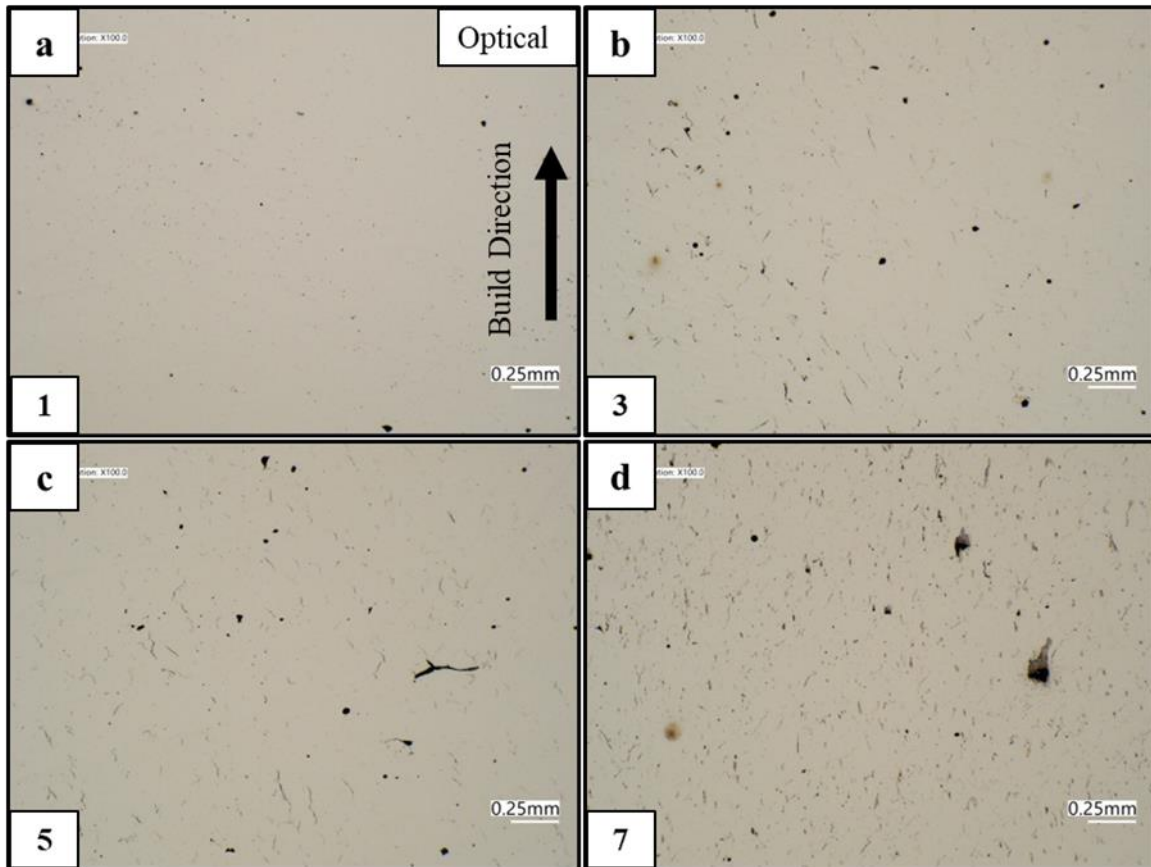


Figure 6: Optical Images of 4 different processing conditions used for D9 alloy. Extensive cracking and other defects can be observed in all the conditions.

While more work couldn't be performed owing to the sample conditions, we still did further analysis via SEM to look at the finer features of the samples. Figure 7 shows the BSE images of sample 3. As expected, the microstructures look very similar to as-deposited SS-316L[32]. At this level of magnification, we weren't able to notice any TiC. Figure 8(d) shows cell structures which have also been noted in previous works on AM 316L.

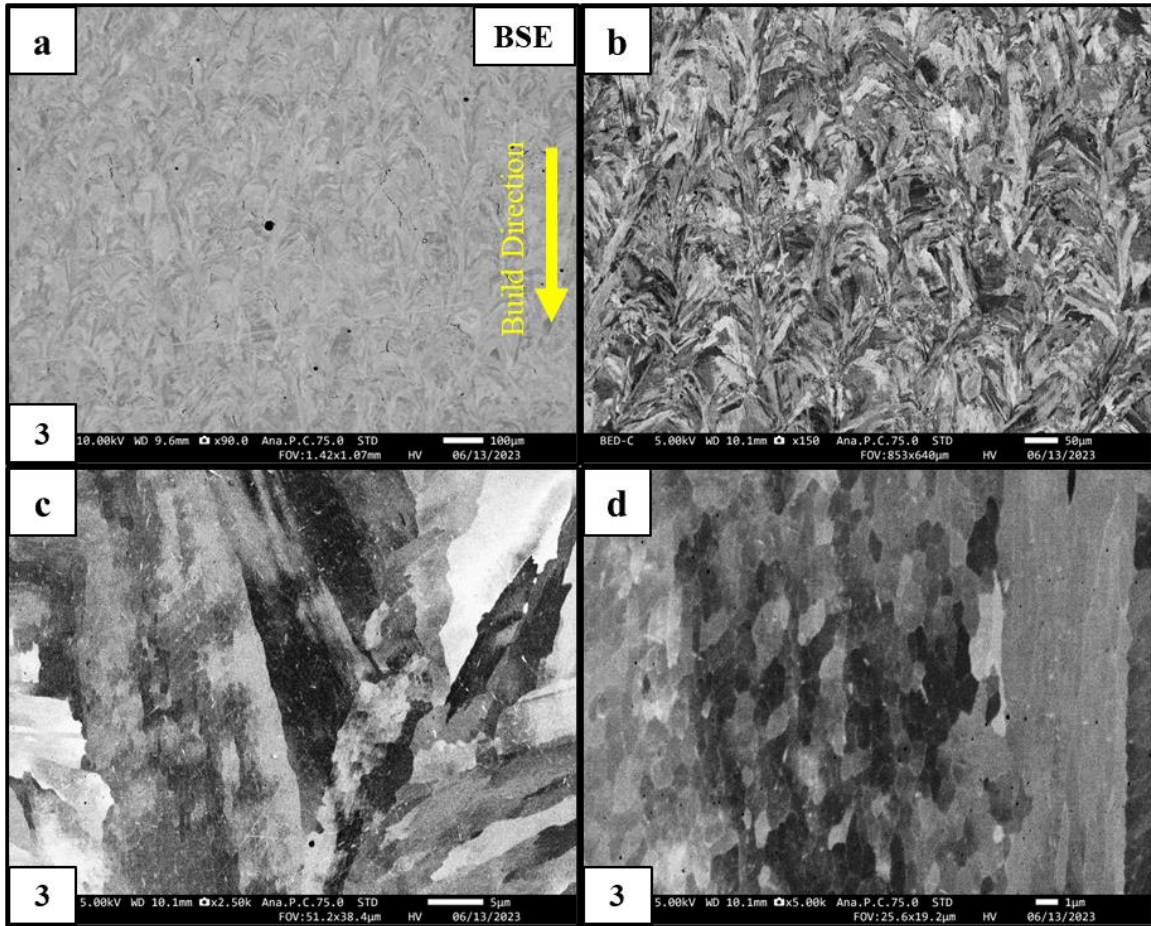


Figure 7: SEM BSE image showing different features of sample condition 3 for D9 alloy. High magnification image in (d) shows cell structures noticed in other SS316 alloys.

EBSD IPF+IQ maps show the grains to be around 50–150 microns, but with no obvious texture present.

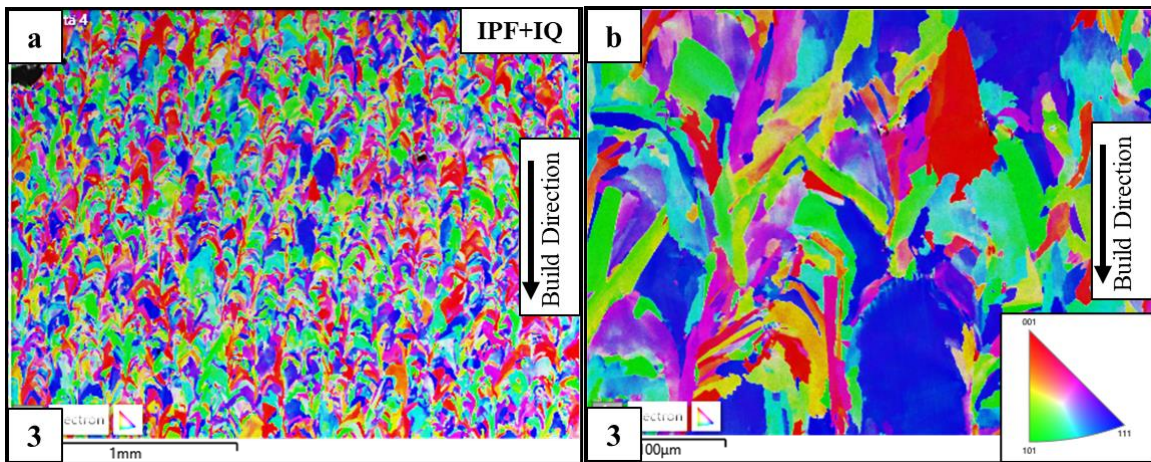


Figure 8: EBSD IPF+IQ map showing grain size and orientation of D9 alloys. Build direction is indicated in the images.

5.2.1.2 Alumina Forming Austenitic Steels (AFA)

Similar to the D9 steels, AFA powder was also very spherical. Higher magnification imaging on individual powder particles, shown in Figure 9 reveals some artefacts on the powder. More work is currently underway to investigate these particles.

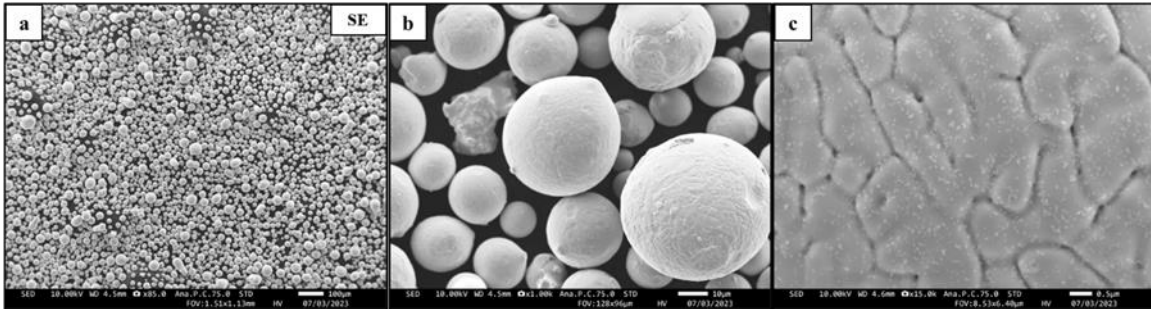


Figure 9: SEM image showing the spherical AFA powders. High magnification image showing artefacts.

As mentioned earlier, significant cracking of the samples was also noted in AFA samples. A few images are shown here. The optical images clearly show the cracking along grain boundaries.

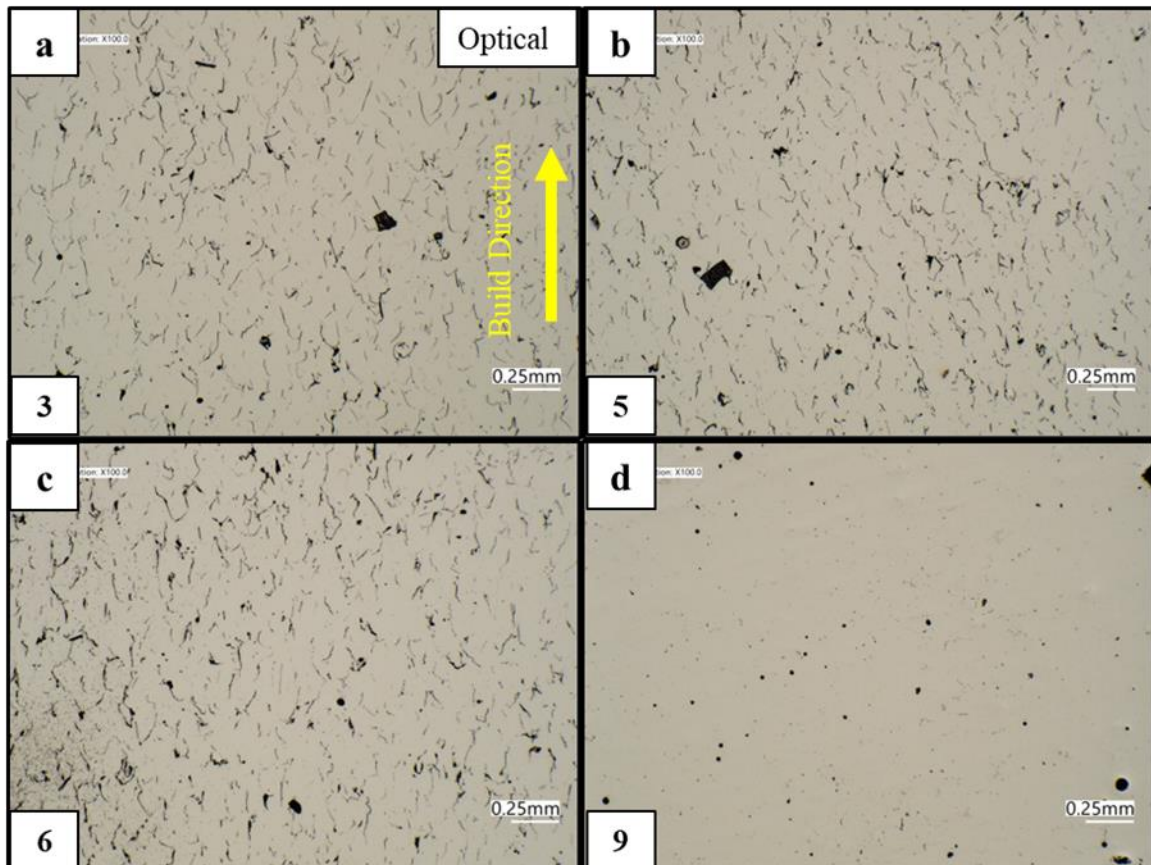


Figure 10: Optical Images of 4 different processing conditions used for AFA alloy. Extensive cracking and other defects can be observed in all the conditions.

Owing to the amount of cracking and other defects in this alloy, currently no further investigation has been performed on this alloy system. Future work includes repeating the same process conditions with a working machine.

5.2.1.3 A709 (NF709)

Figure 11 shows the as received A709 powder with a higher magnification image shown in the inset. The powder can be seen to be spherical, though a few planetary powders exist. Some irregularly shaped particles can also be observed in the high magnification image, though their volume fraction seems to be very low.

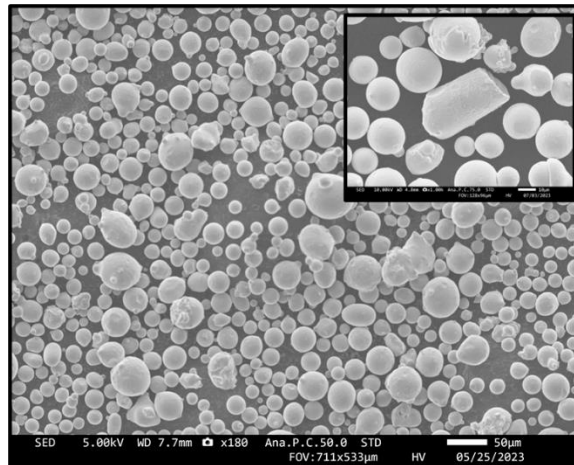


Figure 11: SEM image showing the spherical A709 powders.

Figure 12 shows the optical images of A709. The porosity values calculated using ImageJ are also displayed in these images. For the calculation of porosity, a total of 5 optical images at 100X magnification were taken and the values obtained from ImageJ are averaged out and shown here. As can be seen, in sample 3, which used the recommended condition by Renishaw for 316L SS, almost 99.997% density was achieved. Further investigation is being carried out to verify these values via Archimedes density measurements. Based on the optical images, sample 3 was chosen for further microstructural analysis.

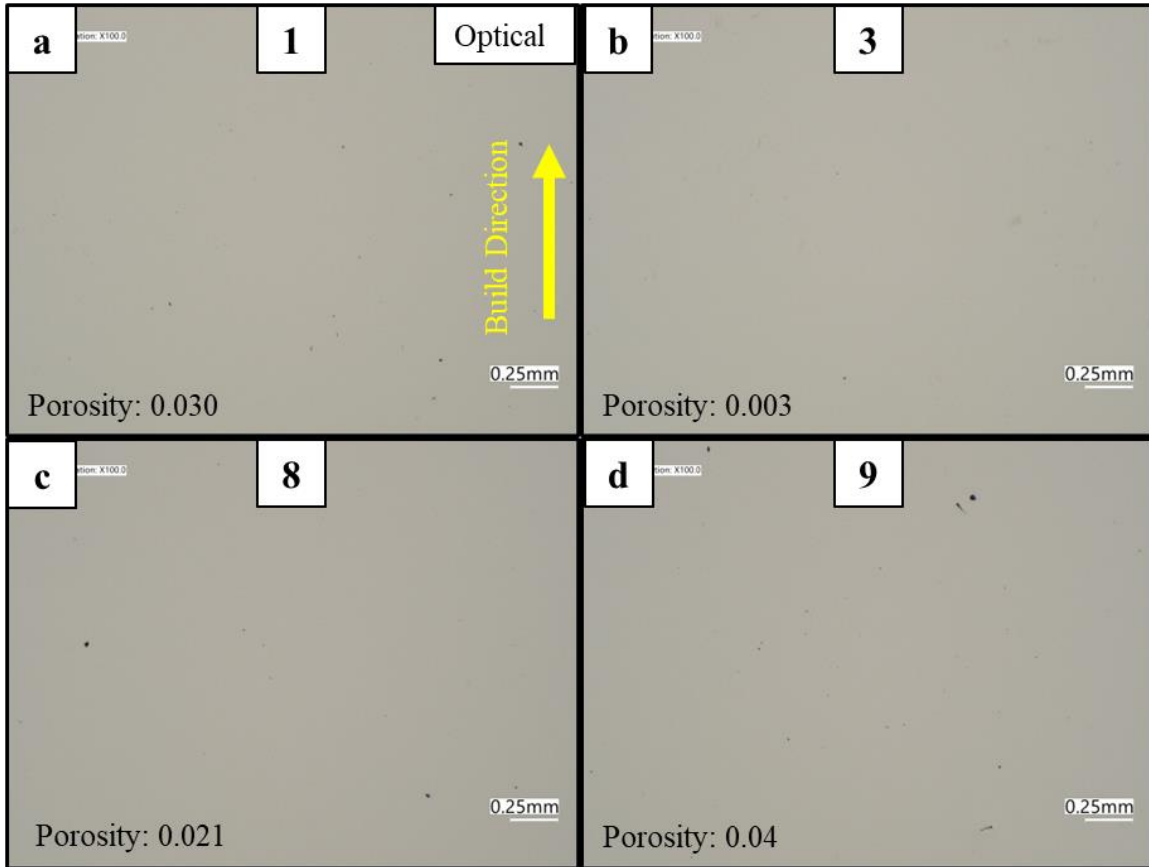


Figure 12: Optical Images of 4 different processing conditions used for A709 alloy. More than 99.5% density was achieved in all conditions.

Figure 13 shows the BSE images of sample 3. Initial image analysis did not reveal the presence of any secondary phases. Interestingly though at higher magnification, cell structures, similar to the ones in D9 steel were also noted in A709 alloy. Some of these cells looked very elongated as shown in Figure 14(b) while the other cells were more equiaxed.

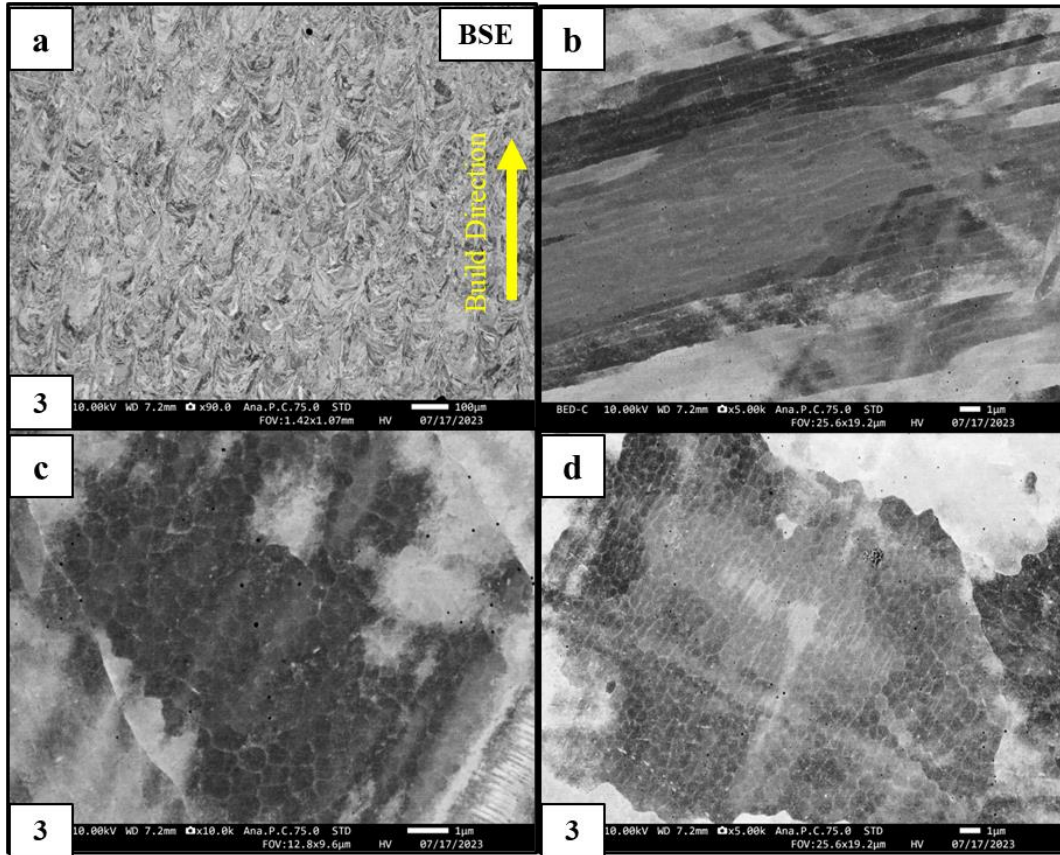


Figure 13: SEM BSE image showing different features of sample A709 alloy. High magnification images shows cell structures noticed in other SS316 alloys.

Similar to the other austenitic stainless steels, FCC grains are clearly noted in the EBSD data shown in Figure 14. There was no obvious texture noted in the sample. The melt pool direction can be clearly seen in the high magnification EBSD images. No other phases were noted.

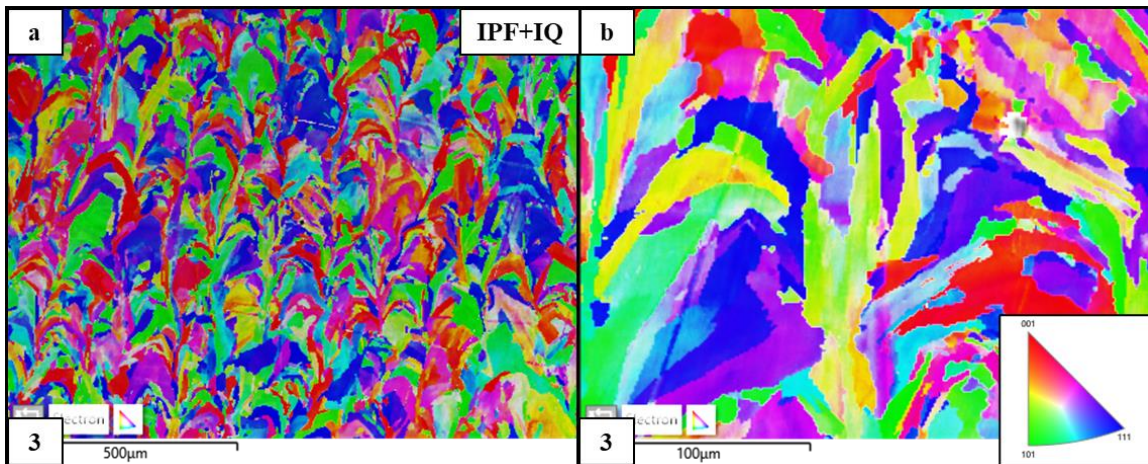


Figure 14: EBSD IPF+IQ map showing grain size and orientation of A709 alloys. No second phase is detected.

5.2.2 Ferritic/Martensitic Steels

It should be noted that, as mentioned in the experimental section, the energy densities (i.e., process parameters) used for F/M steels are higher when compared to Austenitic Steels. This was based on a literature review, which was further corroborated by single track experimental evidence.

5.2.2.1 HT9

Figure 15 shows the powder for HT9. While most of the particles are spherical, there is considerably more difference in morphology, compared to the D9 powder.

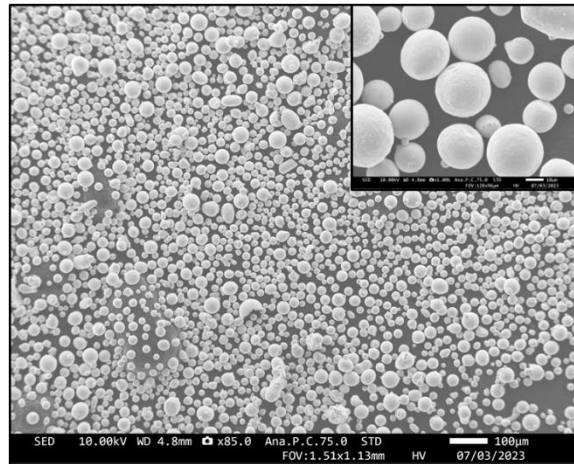


Figure 15: SEM image showing the spherical HT9 powders.

The selected optical images are shown in Figure 16. The microstructures clearly show very little porosity in all the conditions. This proves that the knowledge from single track experiments can potentially be deployed into full scale builds. No other significant features could be seen at this scale. As such electron microscopy was performed on sample 3.

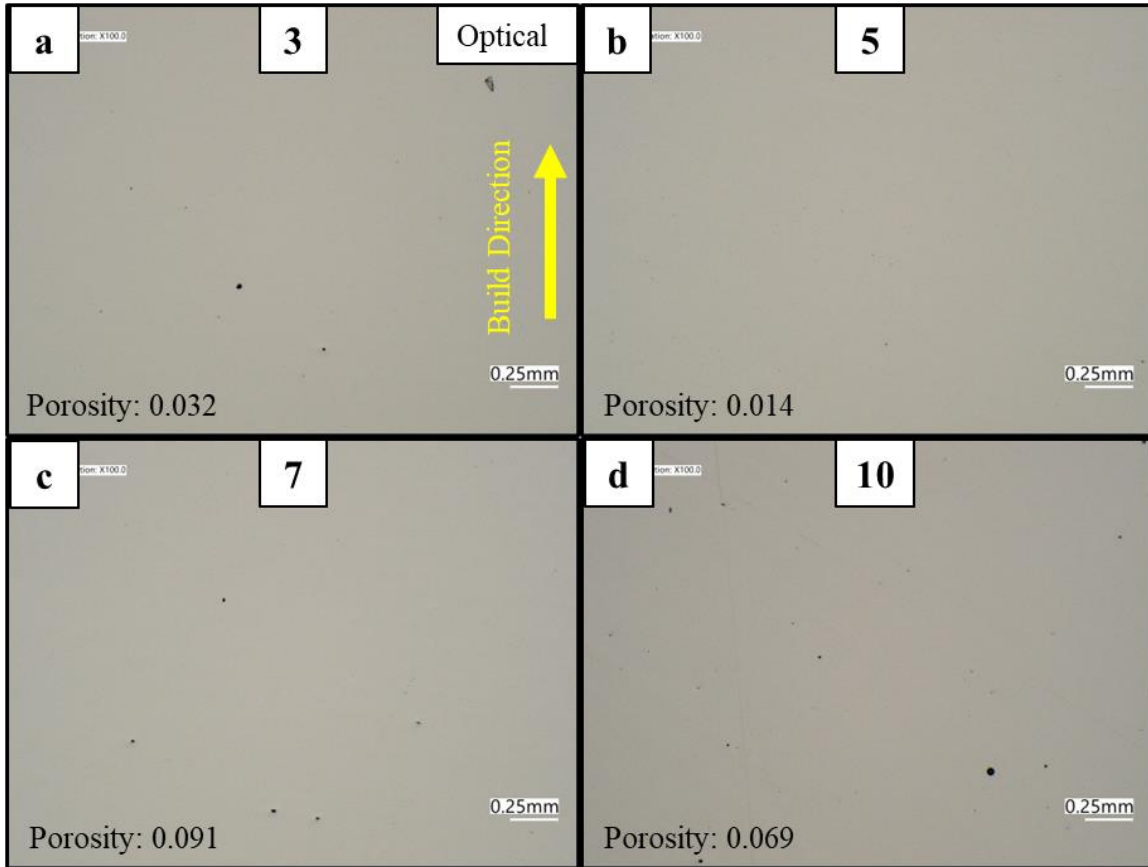


Figure 16: Optical Images of 4 different processing conditions used for HT9 alloy. More than 99.5% density was achieved in all conditions.

The SEM images of sample 3 in Fig. 17 show very interesting features in the HT9 alloy. The images are shown in a way to show higher magnification images of the same features. Clear evidence of the presence of martensite is noted in this system. Interestingly enough the presence of martensite was only observed next to the darker “flower” like features. Further investigation needs to be done to understand this phenomenon better.

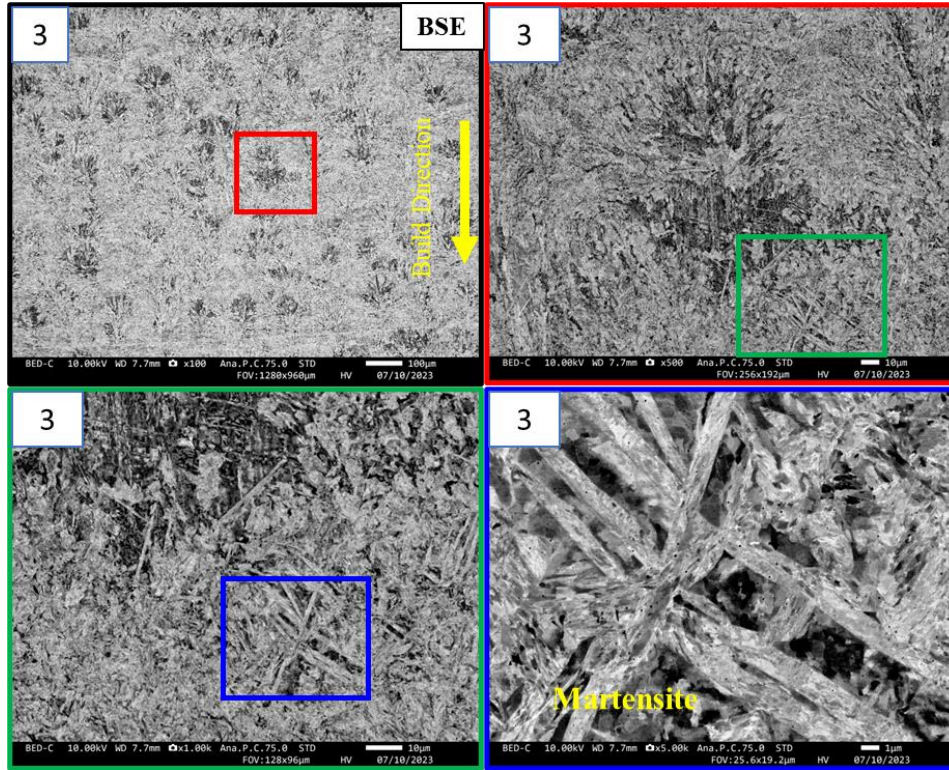


Figure 17: SEM BSE image showing different features of sample condition 3 for HT9 alloy. High magnification image shows clear presence of martensitic laths present in bcc matrix.

Very high magnification EBSD was done on sample 3 to capture the martensite features. Laths in the bottom grain, shown in different colors in Figure 18 are possibly martensitic laths, but more work needs to be done to confirm this. It should also be noted that the matrix here is BCC and the IPF map indicates as such.

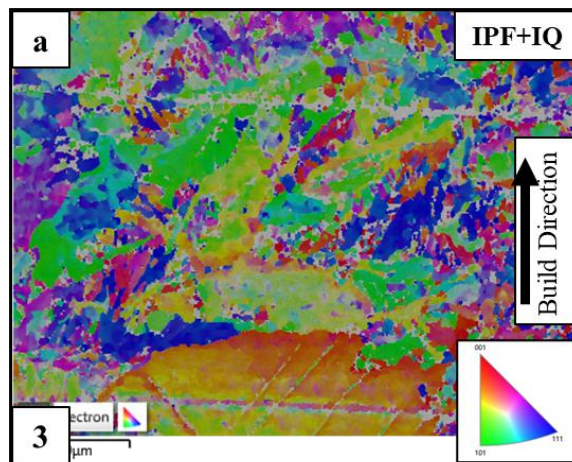


Figure 18: High magnification EBSD IPF+IQ map of HT9 alloy showing grain size and orientation. The un-indexed martensite laths can be seen in the bottom "orange" grain.

5.2.2.2 Grade 91

Figure 19 shows the Grade 91 powder. Similar to D9 sample, there appear to be more planetary particles in this powder.

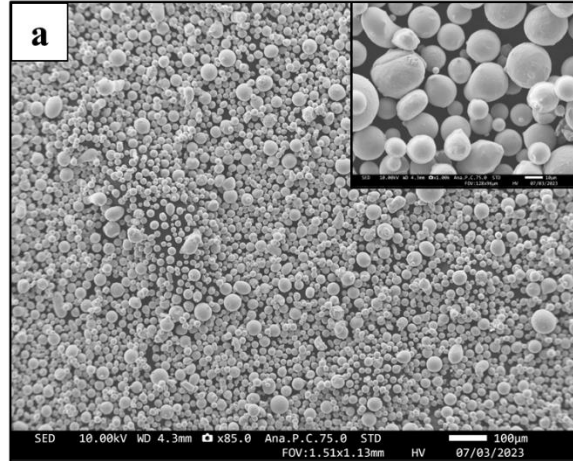


Figure 19: SEM image showing the spherical Grade 91 powders.

For the case of Grade 91 also, the optimized process parameters yielded almost fully dense microstructures, as can be seen in the optical images in Figure 20. Sample 3, which is the optimized condition from LANL[27], shows a porosity of only 0.055.

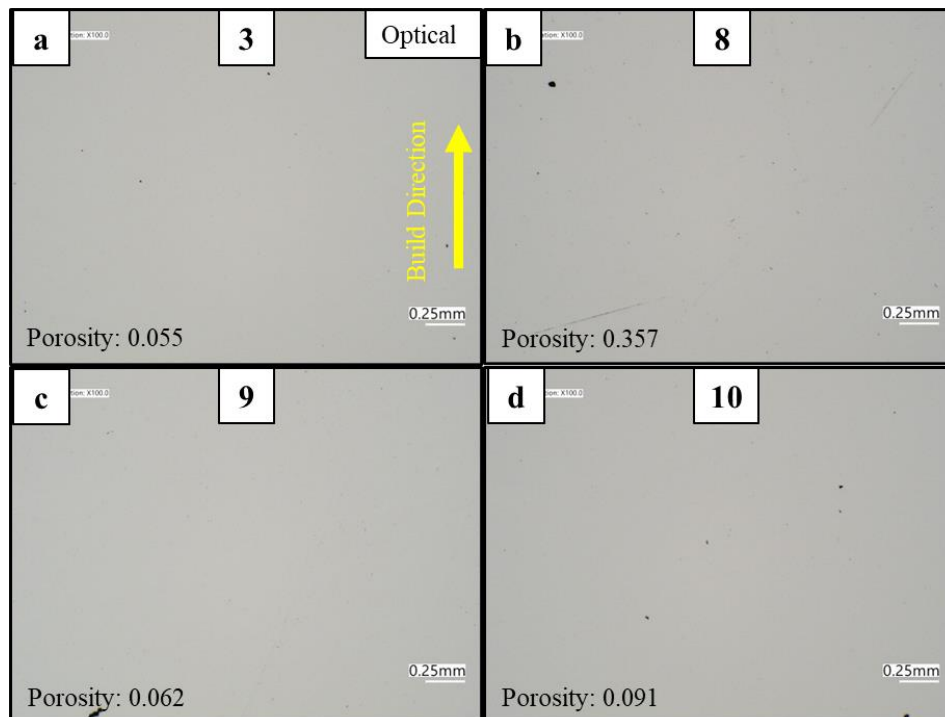


Figure 20: Optical Images of 4 different processing conditions used for Grade 91 alloy. More than 99.5% density was achieved in all conditions.

Similar to all other samples, 5 different optical images are taken for each condition and porosity analyzed via ImageJ and the average is represented here.

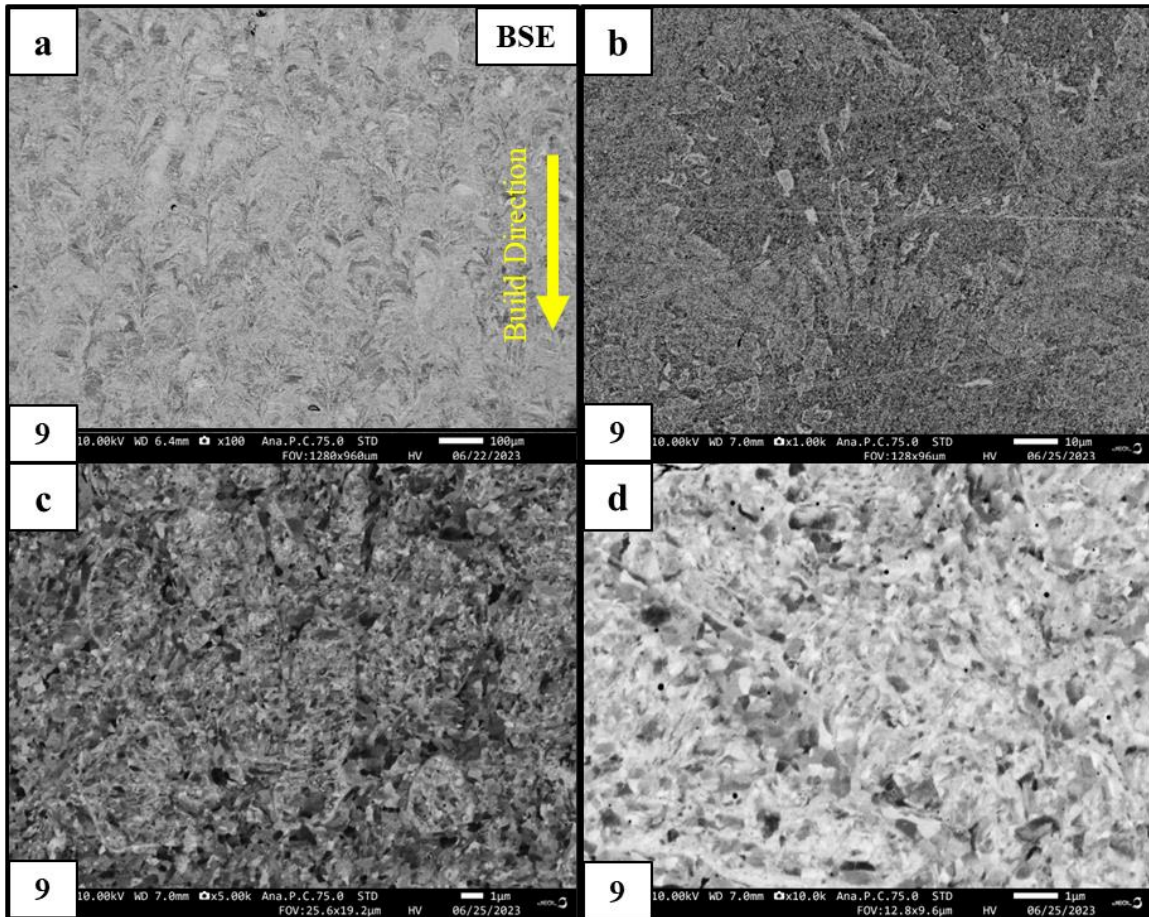


Figure 21: SEM BSE image showing different features of sample condition 9 for Grade 91 alloy. No martensite was noted in this alloy, though very small cells were present throughout.

The SEM images obtained from sample 9 do not show clear evidence of martensite, at least at this length scale. Similar observations were noted by Eftanik et al[28]. Higher magnification images show very fine “cell structures”, different from the dislocation cells observed in the austenitic steels, about 500nm in size. Further investigation is necessary to fully understand the microstructure evolution of this alloy in as-fabricated condition.

The presence of single-phase BCC is confirmed via EBSD analysis shown in Figure 22

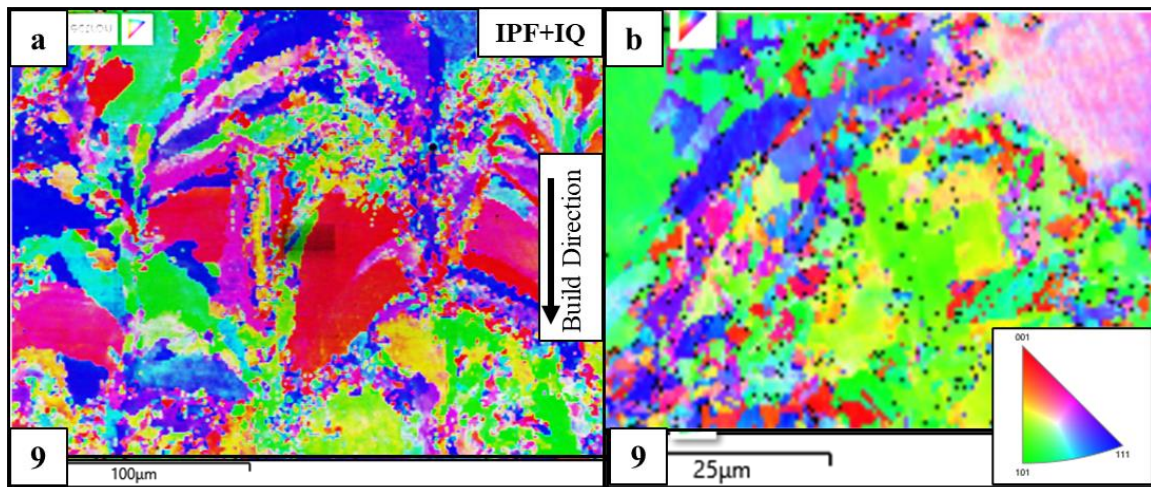


Figure 22: High magnification EBSD IPF+IQ map of sample condition 9 for Grade 91 alloy showing grain size and orientation. No secondary phase is detected.

5.2.2.3 Grade 92

The last alloy discussed in the present work is Grade 92. Figure 23 shows the powder of Grade 92.

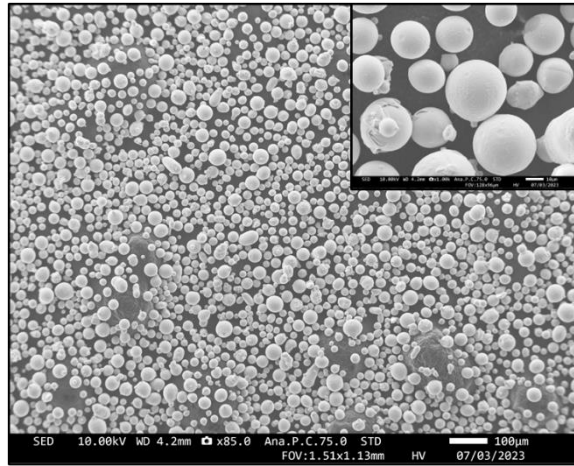


Figure 23: SEM image showing the spherical Grade 92 powder.

For the case of Grade 92 also, the optimized process parameters yielded almost fully dense microstructures, as can be seen in the optical images in Figure 24.

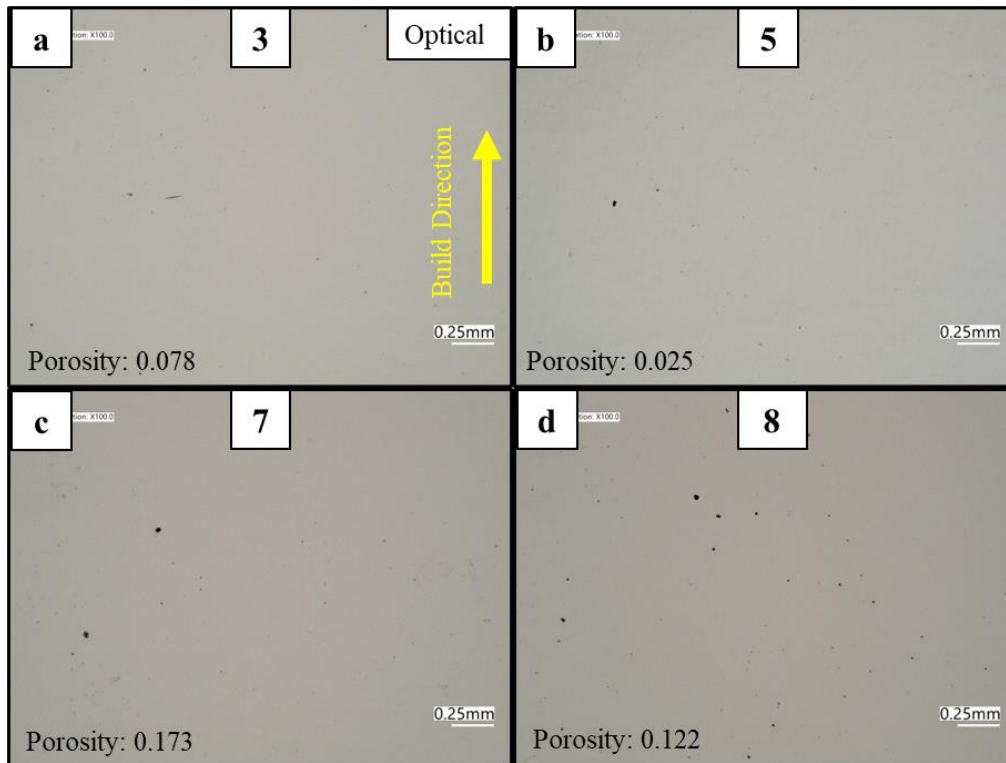


Figure 24: Optical Images of 4 different processing conditions used for Grade 92 alloy. More than 99.5% density was achieved in all conditions.

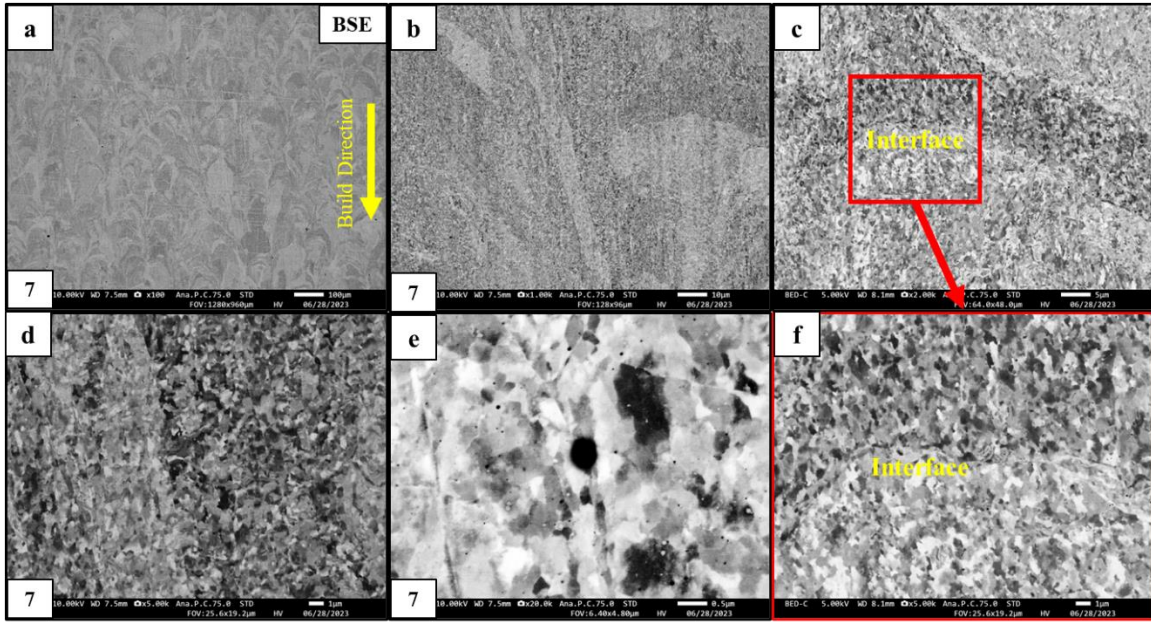


Figure 25: SEM BSE image showing different features of sample condition 7 for Grade 92 alloy. No martensite was noted in this alloy, though very small cells were present throughout.

The SEM images obtained from sample 7 do not show the presence of any evidence of martensite, at least at this length scale, similar to Grade 91. A clear overlap of melt pool boundaries along the build direction can be seen in the images and a change in grain contrast can be observed along the “interface”. Again, like Grade 91, higher magnification images show very fine “cell structures”, about 500nm in size.

Discussions

6.1 Single track experiment

In order to optimize the process parameters for the 3d printing of the alloys, single track experiments with a total of 72 different processing conditions were done for each of the alloy class, i.e., austenitic stainless steels and ferritic/martensitic stainless steels. The dimensions, morphology, overlap etc., of melt pools created by the laser track are used to understand whether the process conditions employed are good. A schematic showing the melt pool overlap and effects of energy density is shown in Figure 26[33]. For a normal condition, adequate penetration and overlap to the previous layers and adjacent melt pools is noted. For conditions which have lower energy density, smaller melt pools are formed, which may lead to lack of fusion between the adjacent melt pools and between layers. If a higher energy density is used, especially with higher powers and lower lasing speeds, this could lead to penetration through many layers causing keyhole issues. [33]. A disrupted melt pool occurs when there is spatter or other inclusions.

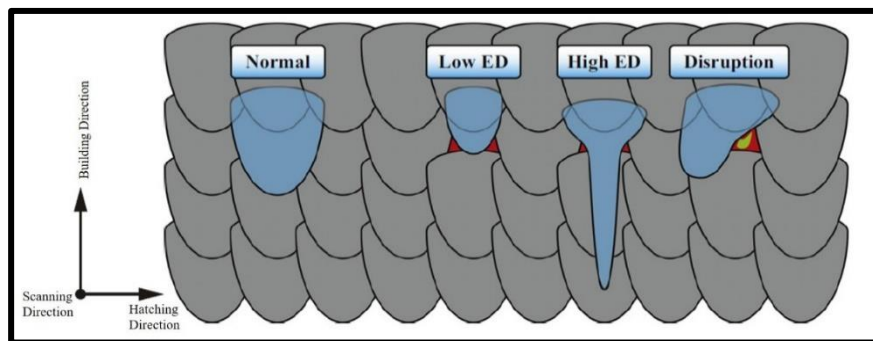


Figure 26: Schematic showing the melt pool overlap and effects of energy density.[33]

The sample with the “ideal condition”, shown in Figure 3, satisfies the criteria for a normal condition mentioned above. The “modified condition”, shown in Figure 4, which has an energy density about 50% higher than the ideal condition shows porosity. Based on these results, a set of parameters to be used for final prints was narrowed down to 10 for each alloy class with the energy density variation $<6.5\%$ for austenitic stainless steels. The energy density variation was maintained for F/M steels.

6.2 Block Build - Austenitic Stainless Steels

The process parameters chosen for printing the three austenitic stainless steels (D9, AFA, and A709) were based off the “ideal conditions” provided by Renishaw for SS-316L. Extensive cracking was noted in both D9 and AFA alloys on the initial prints. Considering the composition differences between SS-316 and D9 is just the minute addition of titanium, it was surprising to see the microstructure of the as built condition. On further inspection it was revealed that the cracking and other defects observed in the sample were not due to the processing conditions, but because of internal issues within the machine. In spite of the cracking, preliminary assessment was performed on the D9 sample. The SEM backscattered images, at this level of magnification, did not reveal the presence of any titanium carbides. Further investigation is necessary, and underway to look at the samples in TEM to look for these carbides. The SEM images show single phase microstructure with cell structures within the grains. This is very commonly reported among SS-316 prints. EBSD analysis was done for phase identification and grain size analysis, and as expected, it shows single phase FCC with grains between 40-120 microns. No obvious texture was noted in the samples.

A709 alloy was printed once the machine issues were fixed and as can be seen from the optical images, almost full density was obtained in some processing conditions. Similar to D9 samples, in the SEM BSE images, no obvious secondary phases were revealed. Cell structures of different sizes and shapes were noted across different grains, and this is shown in Figure 13. EBSD analysis revealed the alloy to have single phase FCC with grains between 40-120 microns in size.

6.3 Block Build - Ferritic/Martensitic Stainless Steels

The processing conditions for F/M steels were based off the work LANL performed on Grade 91 steel in an EoS M290 machine and conditions provided by Renishaw company for 17-4 PH steels. The energy densities used for printing F/M steels were much more varied compared to the austenitic steels, ranging between 50 J/mm³ to 80 J/mm³. In spite of the variation in terms of energy density, all processing conditions yielded almost fully dense parts for all the three alloys. Grade 91 and Grade 92 in the as-deposited condition show single phase BCC with grains around 22-70 microns in size. The presence of martensite wasn't noted in either of the alloys. This is consistent with the previous work published by Eftink et al. and El-Atwani et al.[27], [28]. HT9 on the other hand showed the presence of martensite within the BCC matrix. It was more prominent along the re-heat zones, where a “flowery” feature is noted. More work needs to be done in order

to understand the microstructure evolution of all the three alloy systems. Finite element or Comsol based techniques could potentially be used to understand the heat cycles to justify the microstructures formed in these alloys.

Conclusions and Future Work

7.1 Conclusions

The report summarizes the potential of prioritizing current reactor materials for advanced manufacturing. The following conclusions are drawn from the report.

1. An initial decision criteria matrix was developed with the collaboration of 4 national labs, ANL, PNNL, ORNL, and INL in order to have a consistent and transparent selection process of choosing the existing materials for advanced manufacturing. This was based on extensive literature survey, inputs from industry stakeholders, and expert opinions.
2. A total of 6 alloys, 3 austenitic stainless steels and 3 ferritic martensitic steels were downselected. Once the alloys were selected based on the matrix, obtaining powders for 3D printing proved to be the biggest bottleneck in terms of advancing the work. The powder availability will be of primary concern in future, although obtaining smaller quantities of powders for research will not be financially advisable to industrial scale-up work.
3. Single track experiments were performed on one alloy class each (A709 for austenitic and Grade91 for ferritic/martensitic) to optimize the process parameters for full 3D printed blocks. A total of 72 conditions were used for each of the alloy classes. Characterizing via optical imaging helped narrow down the process parameters for each class.
4. A total of 60 blocks were printed for the initial assessment. 10 different conditions were printed for each of the 6 alloys to see if we could produce defect free, high-density parts. Initial assessment using optical imaging, SEM, and EBSD showed that 4 out of 6 alloys had good consistent microstructures with density >99%. The prints of the AFA and the D9 showed extensive cracking likely due to the lack of control of the chamber atmosphere due to a leaking issue.
5. This exercise proves that the additive manufacturing of the selected Fe-based current reactor materials, either austenitic stainless steel or ferritic/martensitic steels is very feasible, and more work needs to be done in order to understand the microstructure evolution during the depositions and also to further optimize the final microstructures.

7.2 Future Work

Based on the current results and discussions, there are still a few questions which need to be answered, and there is a scope to perform further characterization, for understanding both the microstructural evolution and mechanical behavior.

1. The two alloys which showed cracking and other defects due to the issues with the machine will be printed again using same parameters to isolate the issue and better understand the effect of process parameters on microstructures.
2. Large scale samples of optimized conditions need to be built for mechanical testing including, but not limited to, tensile (room and elevated), creep, and creep fatigue.
3. Post-build treatment and thermal stability of the microstructures needs to be studied.
4. Furthermore, more analysis needs to be done to understand the microstructural evolution in F/M steels. The presence of martensite in HT9 and lack of it Grade 91 and Grade 92 needs to be studied.
5. Irradiation and corrosion testing, time permitting, will also need to be done on the AM samples and compared to their bulk counterparts.

Acknowledgements

This work was sponsored by the U.S. Department of Energy, under Contract No. DE-AC02-06CH11357 with Argonne National Laboratory, managed and operated by UChicago Argonne LLC. The authors acknowledge support for this work from the Advanced Materials and Manufacturing Technologies (AMMT) program with programmatic guidance provided by Meimei Li at Argonne National Laboratory, Ryan Dehoff at Oak Ridge National Laboratory and Dirk Cairns-Gallimore at the Department of Energy.

Chapter 8: References

- [1] W. J. Sames, F. A. List, S. Pannala, R. R. Dehoff, and S. S. Babu, “The metallurgy and processing science of metal additive manufacturing,” *International Materials Reviews*, vol. 61, no. 5, pp. 315–360, 2016, doi: 10.1080/09506608.2015.1116649.
- [2] C. Sun, Y. Wang, M. D. McMurtrey, N. D. Jerred, F. Liou, and J. Li, “Additive manufacturing for energy: A review,” *Appl Energy*, vol. 282, p. 116041, Jan. 2021, doi: 10.1016/J.APENERGY.2020.116041.
- [3] T. J. Maloy and S. Andrew, “Title: Laser Additive Manufacturing of F/M Steels for Radiation Tolerant Nuclear Components Intended for.”
- [4] Li and Meimei, “Advanced Materials and Manufacturing Technologies (AMMT) 2022 Roadmap.” [Online]. Available: www.anl.gov.
- [5] J. J. Lewandowski and M. Seifi, “Metal Additive Manufacturing: A Review of Mechanical Properties,” *Annu Rev Mater Res*, vol. 46, pp. 151–186, Jul. 2016, doi: 10.1146/ANNUREV-MATSCI-070115-032024.
- [6] D. R. Harries, J. Standring, W. D. Barnes, and G. J. Lloyd, “U. K. FAST REACTOR MATERIALS PROGRAMME.,” *ASTM Special Technical Publication*, pp. 1197–1217, 1982, doi: 10.1520/STP34405S.
- [7] T.-L. Sham, Y. Wang, R. Bass, and X. Zhang, “A709 Qualification Plan Update and Mechanical Properties Data Assessment,” 2022. [Online]. Available: <http://www.art.inl.gov>
- [8] “Report on the Initial Loading of SS3 Specimens from the First Commercial Heat of Alloy 709 in Sodium Materials Test Loops for Long-term Exposure Applied Materials Division.” [Online]. Available: www.anl.gov.
- [9] Y. Wang, P. Hou, R. E. Bass, X. Zhang, and T.-L. Sham, “Interim Mechanical Properties Data from FY22 ORNL Testing of A709 with Precipitation Treatment for ASME Code Case Data Package,” 2022. [Online]. Available: www.osti.gov
- [10] F. A. Garner, M. L. Hamilton, C. R. Eiholzer, M. B. Toloczko, and A. S. Kunfar, “INFLUENCE OF COLD WORKLEVEL ON TI4E IRRADIATION CREEP AND CREEP RUPIURE OF TITANIUM-MODIFIED AUSTENITIC STAINLESS STEELS.”
- [11] S. Venkadesan, A. K. Bhaduri, P. Rodriguez, and K. A. Padmanabhan, “Effect of ageing on the microstructural stability of cold-worked titanium-modified 15Cr-15Ni-2.5Mo austenitic

- stainless steel,” *Journal of Nuclear Materials*, vol. 186, no. 2, pp. 177–184, 1992, doi: 10.1016/0022-3115(92)90332-F.
- [12] “CjMF-W06>23-’(t Transient and Static Mechanical Properties of D9 Fuel Pin Cladding and Duct Material Irradiated to High Fluence.”
- [13] A. Banerjee, S. Raju, R. Divakar, E. Mohandas, G. Panneerselvam, and M. P. Antony, “Thermal property characterization of a titanium modified austenitic stainless steel (alloy D9),” *Journal of Nuclear Materials*, vol. 347, no. 1–2, pp. 20–30, Dec. 2005, doi: 10.1016/J.JNUCMAT.2005.06.009.
- [14] W. Zhai, W. Zhou, and S. M. L. Nai, “Grain refinement of 316L stainless steel through in-situ alloying with Ti in additive manufacturing,” *Materials Science and Engineering: A*, vol. 840, Apr. 2022, doi: 10.1016/j.msea.2022.142912.
- [15] S. Bin Han, Y. S. Lee, S. H. Park, and H. Song, “Ti-containing 316L stainless steels with excellent tensile properties fabricated by directed energy deposition additive manufacturing,” *Materials Science and Engineering: A*, vol. 862, Jan. 2023, doi: 10.1016/j.msea.2022.144414.
- [16] R. L. Klueh and A. T. Nelson, “Ferritic/martensitic steels for next-generation reactors,” *Journal of Nuclear Materials*, vol. 371, no. 1–3, pp. 37–52, Sep. 2007, doi: 10.1016/j.jnucmat.2007.05.005.
- [17] N. Sridharan and K. Field, “A Road Map for the Advanced Manufacturing of Ferritic-Martensitic Steels,” *Fusion Science and Technology*, vol. 75, no. 4, pp. 264–274, May 2019, doi: 10.1080/15361055.2019.1577124.
- [18] Y. Chen, “Irradiation effects of HT-9 martensitic steel,” *Nuclear Engineering and Technology*, vol. 45, no. 3, pp. 311–322, 2013, doi: 10.5516/NET.07.2013.706.
- [19] N. Sridharan and K. G. Field, “Preliminary Characterization and Mechanical Performance of Additively Manufactured HT9,” 2018.
- [20] G. Gupta, P. Ampornrat, X. Ren, K. Sridharan, T. R. Allen, and G. S. Was, “Role of grain boundary engineering in the SCC behavior of ferritic-martensitic alloy HT-9,” *Journal of Nuclear Materials*, vol. 361, no. 2-3 SPEC. ISS., pp. 160–173, Apr. 2007, doi: 10.1016/j.jnucmat.2006.12.006.
- [21] P. Xiu *et al.*, “Microchemical evolution of irradiated additive-manufactured HT9,” *Journal of Nuclear Materials*, vol. 559, Feb. 2022, doi: 10.1016/j.jnucmat.2021.153410.

- [22] “Designation: A213/A213M – 19a Standard Specification for Seamless Ferritic and Austenitic Alloy-Steel Boiler, Superheater, and Heat-Exchanger Tubes 1”, doi: 10.1520/A0213_A0213M-19A.
- [23] T. Hatakeyama, K. Sawada, M. Suzuki, and M. Watanabe, “Microstructure development of modified 9Cr-1Mo steel during laser powder bed fusion and heat treatment,” *Addit Manuf*, vol. 61, Jan. 2023, doi: 10.1016/j.addma.2022.103350.
- [24] L. Tan, W. Zhong, Y. Yang, K. G. Field, N. Sridharan, and A. T. Nelson, “Creep behavior of an additively manufactured 9Cr steel in the as-built condition,” *Journal of Nuclear Materials*, vol. 570, Nov. 2022, doi: 10.1016/j.jnucmat.2022.153943.
- [25] J. Feng *et al.*, “Laser additive manufacturing and post-heat treatment on microstructure and mechanical properties of 9Cr steel,” *International Journal of Pressure Vessels and Piping*, vol. 198, Aug. 2022, doi: 10.1016/j.ijpvp.2022.104681.
- [26] W. Zhong *et al.*, “Microstructures and mechanical properties of a modified 9Cr ferritic-martensitic steel in the as-built condition after additive manufacturing,” *Journal of Nuclear Materials*, vol. 545, Mar. 2021, doi: 10.1016/j.jnucmat.2020.152742.
- [27] O. El-Atwani, B. P. Eftink, C. M. Cady, D. R. Coughlin, M. M. Schneider, and S. A. Maloy, “Enhanced mechanical properties of additive manufactured Grade 91 steel,” *Scr Mater*, vol. 199, Jul. 2021, doi: 10.1016/j.scriptamat.2021.113888.
- [28] B. P. Eftink *et al.*, “Tensile properties and microstructure of additively manufactured Grade 91 steel for nuclear applications,” *Journal of Nuclear Materials*, vol. 544, Feb. 2021, doi: 10.1016/j.jnucmat.2020.152723.
- [29] F. Abe, “Precipitate design for creep strengthening of 9% Cr tempered martensitic steel for ultra-supercritical power plants,” *Sci Technol Adv Mater*, vol. 9, no. 1, p. 013002, Jan. 2008, doi: 10.1088/1468-6996/9/1/013002.
- [30] X. Zhou, C. Liu, L. Yu, Y. Liu, and H. Li, “Phase Transformation Behavior and Microstructural Control of High-Cr Martensitic/Ferritic Heat-resistant Steels for Power and Nuclear Plants: A Review,” *J Mater Sci Technol*, vol. 31, no. 3, pp. 235–242, Mar. 2015, doi: 10.1016/J.JMST.2014.12.001.
- [31] C. Cabet, F. Dalle, E. Gaganidze, J. Henry, and H. Tanigawa, “Ferritic-martensitic steels for fission and fusion applications,” *Journal of Nuclear Materials*, vol. 523, pp. 510–537, Sep. 2019, doi: 10.1016/J.JNUCMAT.2019.05.058.

- [32] I. Tolosa, F. Garciandía, F. Zubiri, F. Zapirain, and A. Esnaola, “Study of mechanical properties of AISI 316 stainless steel processed by ‘selective laser melting’, following different manufacturing strategies,” *International Journal of Advanced Manufacturing Technology*, vol. 51, no. 5–8, pp. 639–647, Nov. 2010, doi: 10.1007/s00170-010-2631-5.
- [33] T. Ronneberg, C. M. Davies, and P. A. Hooper, “Revealing relationships between porosity, microstructure and mechanical properties of laser powder bed fusion 316L stainless steel through heat treatment,” *Mater Des*, vol. 189, p. 108481, Apr. 2020, doi: 10.1016/J.MATDES.2020.108481.



Nuclear Science and Engineering Division

Argonne National Laboratory
9700 South Cass Avenue, Bldg. 212
Argonne, IL 60439

www.anl.gov



Argonne National Laboratory is a U.S. Department of Energy
laboratory managed by UChicago Argonne, LLC